A modified Finite Element formulation for the imposition of the slip boundary condition over embedded volumeless geometries

R. Zorrilla[a,b,*], A. Larese[b,c], R. Rossi[a,b]

[a] *Universitat Politècnica de Catalunya (UPC), Departament d'Enginyeria Civil i Ambiental*
[b] *International Center for Numerical Methods in Engineering (CIMNE)*
[c] *Università degli Studi di Padova, Department of Mathematics*

Abstract

This work describes a novel formulation for the simulation of Navier-Stokes problems including embedded objects. The new proposal is based on the use of a modified finite element space, which replaces the standard one within the elements intersected by the immersed geometry. The modified space is able to exactly reproduce the jumps happening at the embedded boundary while preserving the conformity across the faces intersected by the embedded object. The paper focuses particularly on the imposition of a slip boundary condition on the surface of the embedded geometry, proposing a new technique for the application of such constraint. The new proposal is carefully benchmarked using the results of a body fitted technique and of an alternative embedded approach. Potential applications of interest are also presented.

Keywords: Embedded boundary methods, Immersed boundary methods, Navier-Stokes, Volumeless bodies, Slip boundary condition, Discontinuous shape functions

2010 MSC: 00-01, 99-00

*Corresponding author
Email addresses: rzorrilla@cimne.upc.edu (R. Zorrilla), antonia.larese@unipd.it (A. Larese), rrossi@cimne.upc.edu (R. Rossi)

1. Introduction

The Computational Fluid Dynamics (CFD) simulation of the fluid flow around objects is typically achieved by the construction of a volume discretization that matches the geometry of the body of interest as closely as possible. This gives rise to the so called body-fitted discretization. While seeming appealing, such approaches have obvious limitations, that become apparent for the simulation of moving bodies. The need of overcoming such limitations has lead to the development of a variety of alternative methods, such as the Immersed Boundary Method (IBM) [1][2] or the Embedded Boundary Method (EBM). Such techniques make it possible to automatically include arbitrary, possibly moving, bodies into the fluid domain, and to account for their interaction with the fluid flow. The crucial difference with respect to the body-fitted alternatives is that the analysed body and the fluid are discretized separately. While performing the simulation, the body is overlapped onto the fluid domain at the position of interest. An automatic intersection is performed, typically by employing a level set technique [3], to implicitly represent the object of interest in the fluid domain.

While the use of an unfitted approach inevitably introduces complexities into the formulation, the resulting methods can overcome some of the difficulties associated with the conforming counterparts. For example, while it is possible to employ Arbitrary Lagrangian-Eulerian (ALE) techniques [4][5], large displacements and rotations of the body typically yield to extremely distorted (or even inverted) elements, practically limiting the use of ALE solutions to relatively small boundary movements. Such limitation does not exist for fixed mesh methods, which can handle arbitrarily large displacements and rotations, or even changes in the topology (simply impossible for ALE techniques), by updating the level set representation in accordance to the movement of the body.

Furthermore, since the geometric distance computation is a robust operation, the level set based approaches open new possibilities to directly include the exact CAD geometry (involving trimmed NURBS) into the simulation pipeline or to

simulate "dirty" geometries. This is because the distance computation from a NURBS surface is an operation as robust as computing the distance from a lower order discretization. Furthermore, the use of a level set approach intrinsically filters out the geometric details that cannot be represented by the volume mesh, improving the robustness and speed of the model preparation phase. Taking into account that the model preparation of realistic engineering problems is known to amount to more than the 50% of the total analysis time [6], this is clearly an important advantage, particularly considering that the details can always be recovered upon refinement. Moreover, the mesh generation step is typically more robust since the mesh is not required to comply with the details of the body geometry. Lastly, the model preparation can also benefit from the use of fast octree mesh generators [7] to provide initial meshes which can be then improved by the use of mesh adaptation techniques [8][9].

A rather large literature study the use of fixed mesh approaches to solve complex incompressible Navier-Stokes (N-S) problems. For instance, the IBM is successfully applied to model a helicon ribbon mixer problem in [10]. This method is also employed in [11] for solving complex real engineering geometries without need to modify the input files before the mesh generation.

In the literature, the distinction between "Immersed" and "Embedded" techniques tends to be blurry and different authors may provide a different definition. For the sake of clarity, we will use the term "Immersed" when the Solid-Fluid coupling is performed by imposing a constraint over the entire overlapping zone between the domains and the term "Embedded" when the coupling is enforced at the frontier between solid and fluid.

According to such definition, even though the IBM out stands for its robustness and implementation simplicity, it may lack precision in some applications, since the boundary condition is not directly enforced over the interface cut. Instead of that, the immersed object velocity is directly imposed on those fluid nodes lying on the interior of the object, making it impossible to recover the original interface.

On the contrary, EBM relies on applying the boundary conditions over the

interface cut. This is commonly done in a weak sense by using techniques such as the penalty method or the Nitsche method [12]. In [13], the authors apply a modified Nitsche method to impose the no-slip boundary condition to the N-S equations. In [14], a stabilized Nitsche method is used for the imposition of the no-slip boundary condition to the Stokes equations. A similar technique is applied in [15] for the Oseen equations. Regarding the slip boundary condition, Lagrange multipliers technique as well as the Nitsche method are used to apply the slip boundary condition to the Stokes equations in [16]. This is extended to apply a general Navier-slip boundary condition to the N-S equations in [17]. In [18], the authors present an innovative approach where a spline-based surface is directly immersed in the fluid domain to impose a Nitsche no-slip boundary condition.

A common feature of the above highlighted formulations is the need for a well-defined internal volume. This turns into a limitation when shell or membrane bodies, such as lightweight structures, biological tissues or boat sails, need to be analysed. Multiple works address this limitation by adding a volume force that modifies the flow pattern in accordance to the embedded volumeless geometry [1][19][20]. Even though this is probably the most straightforward approach, it is difficult to represent the flow discontinuities as well as to precisely compute the required volume force value. An alternative based on adding the immersed bodies dynamics to the flow dynamics to model embedded moving fibres is presented in [21]. More complex approaches also exist, as the one presented in [22], which uses a fractional step ghost cell method for representing complex moving geometries. While the method presented in [22] works for any type of geometry (with/without internal volume), it requires the neighbour elements for the imposition of the boundary conditions. As it is widely known, the implementation of this kind of operations becomes even more cumbersome in a distributed memory environment (MPI).

The aim of the current work is to present a generalized unfitted technique which is able to overcome all the previously commented limitations. The proposal takes the idea from the use of the discontinuous space investigated in [23].

Our proposal makes possible to represent discontinuities in the fluid flow, so it is suitable not only for the simulation of bodies with a well defined volume but also for volumeless ones. Besides, the formulation is purely elemental and therefore easily extensible to the use of a distributed memory environment.

A classical difficulty of embedded approaches is the lack of resolution in the vicinity of the body, which impedes the correct simulation of viscous effects close to the body surface. Current work proposes a technique for the imposition of the slip boundary condition on embedded boundaries. While, from a theoretical point of view the use of a slip BC is only well defined for inviscid fluids, the slip approximation is good for high Reynolds (Re) flows [24]. In that work, the results of the viscous-slip approach are compared with experimental data, confirming that this combination is a valid alternative when a high boundary layer resolution is not required. Apart from the high-Re scenarios, the slip approximation is also relevant for some highly viscous flows applications. For example it could be an alternative to consider the effect of lubrication on the domain boundaries (lubrication is indeed applied with the exact purpose of avoiding a stick condition between the viscous fluid and the walls).

All the formulations discussed in this work have been implemented within the Kratos Multiphysics open source framework [25] [26].

2. Methodology

Firstly, the governing equations are presented and the finite element formulation is derived using an automatic differentiation technique. After that, the approaches to impose the slip boundary condition are described. Special emphasis is put on the one proposed by the authors, which uses an alternative set of shape functions (henceforth named "Ausas" shape functions after the name of the original author).

2.1. The Navier-Stokes equations

In this work we focus on the incompressible Navier-Stokes equations for Newtonian fluids. The Cauchy stress tensor $\boldsymbol{\sigma}$ is defined as $\boldsymbol{\sigma} = -p\mathbf{I} + \mathbb{C} : \boldsymbol{\nabla}^s \mathbf{u}$,

where $\mathbf{u}$ is the velocity, p the pressure, $\boldsymbol{\nabla}^s$ the symmetric gradient operator and $\mathbb{C}$ the the constitutive tensor describing the viscous behaviour. By substituting $\boldsymbol{\sigma}$ into the balance of linear momentum and mass conservation equations yields the well-known viscous incompressible Navier-Stokes equations

$$\rho \frac{\partial \mathbf{u}}{\partial t} + \rho \mathbf{u} \cdot \boldsymbol{\nabla} \mathbf{u} - \boldsymbol{\nabla} \cdot (\mathbb{C} : \boldsymbol{\nabla}^s \mathbf{u}) + \boldsymbol{\nabla} p = \rho \mathbf{b} \tag{1a}$$

$$\frac{D\rho}{Dt} + \rho \boldsymbol{\nabla} \cdot \mathbf{u} = 0 \tag{1b}$$

where ρ the density and $\mathbf{b}$ the body force. The operator $\partial(\bullet)/\partial t$ is the partial time derivative and $\boldsymbol{\nabla}$ is the gradient operator.

For purely incompressible fluids, it is customary to assume $\frac{D\rho}{Dt} = 0$. This implies that the pressure is defined up to a constant, which is typically fixed once a Neumann boundary condition is imposed. Unfortunately, this feature becomes problematic when dealing with poorly defined input geometries or moving boundaries since isolated closed domains of fluid (with no Neumann Boundary) may appear.

This issue is readily fixed if a slight compressibility is included in the formulation. In particular if we assume the simplified equation of state $p = \rho c^2 \implies c^2 = \partial p / \partial \rho$, which is valid for almost incompressible fluids, we can rewrite the density time derivative in terms of the pressure as

$$\frac{D\rho}{Dt} + \rho \boldsymbol{\nabla} \cdot \mathbf{u} = 0 \longrightarrow \frac{\partial \rho}{\partial p} \frac{Dp}{Dt} + \rho \boldsymbol{\nabla} \cdot \mathbf{u} = 0 \longrightarrow \frac{1}{c^2} \frac{Dp}{Dt} + \rho \boldsymbol{\nabla} \cdot \mathbf{u} = 0 \tag{2}$$

If we further assume that $\boldsymbol{\nabla} \rho \approx \mathbf{0}$, physically expressing that density fluctuations are negligible, the term $\mathbf{u} \cdot \boldsymbol{\nabla} \rho$ can be neglected to give

$$\frac{1}{\rho c^2} \frac{\partial p}{\partial t} + \boldsymbol{\nabla} \cdot \mathbf{u} = 0 \tag{3}$$

The final form of the governing equations is thus

$$\rho \frac{\partial \mathbf{u}}{\partial t} + \rho \mathbf{u} \cdot \boldsymbol{\nabla} \mathbf{u} - \boldsymbol{\nabla} \cdot (\mathbb{C} : \boldsymbol{\nabla}^s \mathbf{u}) + \boldsymbol{\nabla} p = \rho \mathbf{b} \tag{4a}$$

$$\frac{1}{\rho c^2} \frac{\partial p}{\partial t} + \boldsymbol{\nabla} \cdot \mathbf{u} = 0 \tag{4b}$$

Note that the single-fluid fully-incompressible form $\nabla \cdot \mathbf{u} = 0$ is recovered if the sound speed $c \to \infty$. Specifically, the compressibility is not needed for the

examples presented in the current work. Hence through the paper the speed of sound is taken as 10^{12}m/s, so that the compressibility is effectively negligible in all of the discussed cases. However, the option to employ a higher value is left to the user.

2.2. Discrete form and stabilization

In the current work, only simplicial elements are considered. It is widely known that these elements do not satisfy the *inf-sup condition* and the use of a stabilization method is therefore required. There exist several alternatives that are proved to be effective for similar problems. Among those techniques, we can mention the Finite Increment Calculus (FIC) [27], the Streamline upwind/Petrov-Galerkin (SUPG) [28] and the Variational Multiscales Method (VMS) [29] [30]. We adopt the VMS method, which relies on the separation of the solution fields $(\mathbf{u}, p)$ in two scales as

$$\mathbf{u} = \mathbf{u_h} + \mathbf{u_s} \tag{5a}$$

$$p = p_h + p_s \tag{5b}$$

The first (Eq. 5) is the FE resolvable scale $(\mathbf{u_h}, p_h)$. The second one, referred to as the subscale $(\mathbf{u_s}, p_s)$, represents the fluctuations that cannot be captured by the FE solution. After inserting Eq. 5 into the N-S equations (Eq. 4), the governing equations of the problem read

$$\begin{aligned} &\rho \frac{\partial \left(\mathbf{u_h} + \mathbf{u_s}\right)}{\partial t} + \rho \left(\mathbf{u_h} + \mathbf{u_s}\right) \cdot \boldsymbol{\nabla} \left(\mathbf{u_s} + \mathbf{u_s}\right) \\ &\quad - \boldsymbol{\nabla} \cdot \left(\mathbb{C} : \boldsymbol{\nabla}^s \left(\mathbf{u_h} + \mathbf{u_s}\right)\right) + \boldsymbol{\nabla} \left(p_h + p_s\right) = \rho \mathbf{b} \end{aligned} \tag{6a}$$

$$\frac{1}{\rho c^2} \frac{\partial \left(p_h + p_s\right)}{\partial t} + \boldsymbol{\nabla} \cdot \left(\mathbf{u_h} + \mathbf{u_s}\right) = 0 \tag{6b}$$

Different models for the subscale are presented in the literature. In general terms, we can say that the subscales are normally expressed as a projection of the FE residuals onto the space of the small scales. Depending on the nature of this projection, the Algebraic Sub-Grid Scales (ASGS)[31] or the Orthogonal Sub-Grid Scales (OSS)[32] are obtained. In this work, the ASGS technique is

selected. This method recovers the velocity ($\mathbf{u_s}$) and pressure (p_s) subscales by using an algebraic approach based on the FE velocity ($\mathbf{u_h}$) and pressure (p_h) solutions as

$$\mathbf{u_s} = \tau_1 \mathbf{R^M}(\mathbf{u_h}, p_h) \tag{7a}$$

$$p_s = \tau_2 R^C(\mathbf{u_h}, p_h) \tag{7b}$$

where $\mathbf{R^M}$ and R^C are the residuals of the momentum and mass conservation equations. Note that the subscale dependency on the FE solution is introduced by such residuals of the governing equations, which are defined as

$$\mathbf{R^M}(\mathbf{u_h}, p_h) = \rho \mathbf{b} - \rho \frac{\partial \mathbf{u_h}}{\partial t} - \rho \mathbf{u_h} \cdot \boldsymbol{\nabla} \mathbf{u_h} + \boldsymbol{\nabla} \cdot (\mathbb{C} : \boldsymbol{\nabla}^s \mathbf{u_h}) - \boldsymbol{\nabla} p_h \tag{8a}$$

$$R^C(\mathbf{u_h}, p_h) = -\frac{1}{\rho c^2} \frac{\partial p_h}{\partial t} - \boldsymbol{\nabla} \cdot \mathbf{u_h} \tag{8b}$$

Eq. 6 shows that the subscales are time dependent, leading to a so called *dynamic subscales formulation*. If this time dependency is neglected by assuming that $\partial \mathbf{u_s}/\partial t \approx \mathbf{0}$ and $\partial p_s/\partial t \approx 0$, a *quasi-static subscales formulation* is obtained. Even though the dynamic approach has somewhat superior characteristics [33], these come at the cost of additional complexity in the formulation as well as of increased memory consumption and computational effort, which lead us to prefer the use of the quasi-static approach.

Both $\mathbf{u_s}$ and p_s are assumed to be such that their boundary integrals are 0. The stabilization constants τ_1 (Eq. 9a) and τ_2 (Eq. 9b) are taken from [31]. These are defined as

$$\tau_1 = \left(\frac{\rho \tau_{dyn}}{\Delta t} + \frac{c_2 \rho \|\mathbf{u_h}\|}{h} + \frac{c_1 \mu}{h^2} \right)^{-1} \tag{9a}$$

$$\tau_2 = \frac{h^2}{c_1 \tau_1} \tag{9b}$$

where τ_{dyn} is a parameter bounded between 0 and 1. $c_1 = 4.0$ and $c_2 = 2.0$ are the stabilization constants, $\|\mathbf{u}\|$ is the convective velocity norm, μ is the dynamic viscosity and h is the element size. In this work h is always computed as the average of the heights associated to each node of the element.

2.3. Automatic differentiation

Once the governing Partial Differential Equations (PDE) are defined, we proceed to discretize the problem, which we cast in residual form.

By using the standard notation $(\bullet, \bullet)_\Omega$ to denote the inner product volume integral, the discrete FE functional can be defined as

$$\Psi\left(\mathbf{w}, q, \mathbf{u}, p\right) := \left(\mathbf{w}, \mathbf{R}^{\mathbf{M}}(\mathbf{u}, p)\right)_\Omega + \left(q, R^C(\mathbf{u}, p)\right)_\Omega \tag{10}$$

where $\mathbf{w}$ and q are the velocity and pressure test functions.

Substituting the momentum and mass conservation residuals, together with the solution decomposition in Eq. 5, into the Galerkin functional (Eq. 10) yields the Navier-Stokes functional to be solved

$$\begin{aligned}(\mathbf{w}, \rho\mathbf{b})_\Omega - \left(\mathbf{w}, \rho\frac{\partial \mathbf{u_h}}{\partial t}\right)_\Omega - (\mathbf{w}, \rho\mathbf{u_h}\cdot\boldsymbol{\nabla}(\mathbf{u_h}+\mathbf{u_s}))_\Omega \\ + (\mathbf{w}, \boldsymbol{\nabla}\cdot(\mathbb{C}:\boldsymbol{\nabla}^s(\mathbf{u_h}+\mathbf{u_s})))_\Omega - (\mathbf{w}, \boldsymbol{\nabla}(p_h+p_s))_\Omega \\ - \left(q, \frac{1}{\rho c^2}\frac{\partial p_h}{\partial t}\right)_\Omega - (q, \boldsymbol{\nabla}\cdot(\mathbf{u_h}+\mathbf{u_s}))_\Omega = 0\end{aligned} \tag{11}$$

where the quasi-static subscales model is already taken into consideration. After integrating by parts, the previous Navier-Stokes functional reads

$$\begin{aligned}&(\mathbf{w}, \rho\mathbf{b})_\Omega - \left(\mathbf{w}, \rho\frac{\partial \mathbf{u_h}}{\partial t}\right)_\Omega - (\mathbf{w}, \rho\mathbf{u_h}\cdot\boldsymbol{\nabla}\mathbf{u_h})_\Omega - (\boldsymbol{\nabla}^s\mathbf{w}, \mathbb{C}:\boldsymbol{\nabla}^s\mathbf{u_h})_\Omega \\ &+ (\boldsymbol{\nabla}\cdot\mathbf{w}, p_h)_\Omega - \left(q, \frac{1}{\rho c^2}\frac{\partial p_h}{\partial t}\right)_\Omega - (q, \boldsymbol{\nabla}\cdot\mathbf{u_h})_\Omega + \langle\mathbf{w}, \mathbf{t}\rangle_\Gamma \\ &+ (\rho\mathbf{u_h}\boldsymbol{\nabla}\mathbf{w}, \mathbf{u_s})_\Omega + (\rho(\boldsymbol{\nabla}\cdot\mathbf{u_h})\mathbf{w}, \mathbf{u_s})_\Omega + (\boldsymbol{\nabla}\cdot\mathbf{w}, p_s)_\Omega + (\boldsymbol{\nabla}q, \mathbf{u_s})_\Omega = 0\end{aligned} \tag{12}$$

where the dot product boundary integral is denoted as $\langle\bullet, \bullet\rangle_\Gamma$, with $\mathbf{t}$ being the Cauchy traction vector, computed as $\mathbf{t} = (\mathbb{C}:\boldsymbol{\nabla}^s\mathbf{u_h} - p_h\mathbf{I})\cdot\mathbf{n}$, and $\mathbf{n}$ the boundary outwards unit vector. Note that the null boundary value of the subscales assumption is considered here.

The discrete functional (Eq. 12) is then symbolically implemented in Python using the Computer Algebra System (CAS) library *Sympy* [34]. To automatically obtain the elemental Left Hand Side (**LHS**) and Right Hand Side (**RHS**), the symbolic functional needs to be expressed in terms of the nodal test functions ($\mathbf{w}_I$ and q_I) and of the nodal unknowns ($\mathbf{u}_I$ and p_I). Then, by assuming

a symbolic description of the shape functions and of their derivatives, the elemental **RHS** is obtained by symbolic differentiation as

$$\mathbf{RHS}_I = \frac{\partial \Psi \left(\mathbf{w}, q, \mathbf{u}, p \right)}{\partial \left(\mathbf{w}_I, q_I \right)} \tag{13}$$

while the elemental **LHS** is similarly obtained as

$$\mathbf{LHS}_{IJ} = -\frac{\partial \mathbf{RHS}_I}{\partial \left(\mathbf{u}_{\mathbf{h},J}, p_{h,J} \right)} \tag{14}$$

2.4. Embedded formulations and immersed bodies representation

The main distinguishing feature of embedded (or immersed) approaches with respect to body fitted alternatives is that the domain is meshed without taking into account the geometry of the analysed bodies. Instead, the object representation is achieved by the use of a level set function [3] defined as the signed distance to the object skin, which guarantees that the body shape can be recovered as the zero iso-surface of the level set field.

Considering the nature of the analysed bodies, the distance functions can be roughly divided in two types. The first type is used to describe those objects that have a well-defined internal volume (e.g. aerofoils). These bodies can be represented using a continuous signed distance function. As depicted in Fig. 1, such function takes a positive value in the fluid domain nodes (light green) or a negative one in the structure domain nodes (red). The zero isosurface (dashed line) is therefore the immersed object skin representation.

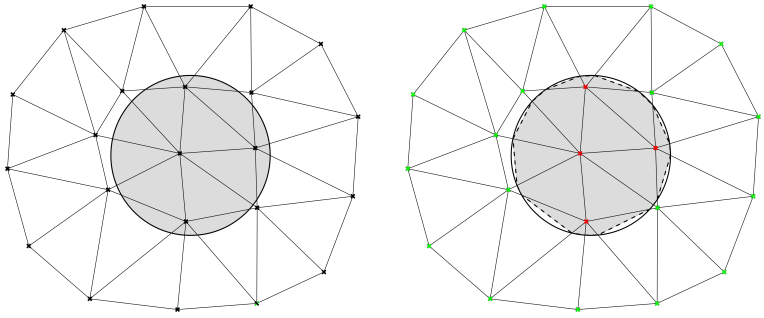

Figure 1: Continuous distance function. Body with a well-defined internal volume (left) and continuous distance representation (right).

The second type is used for representing bodies without internal volume (e.g. boat sails). This kind of geometries cannot be represented by a continuous distance function since no intersections could be found. This limitation can be overcome using a discontinuous distance field, which is computed (and stored) element by element, meaning that the same node can have different distance values depending on the element considered. Such feature is what makes the distance function discontinuous and allows tracking such volume-less geometries. Figure 2 shows a qualitative example of this elemental distance function. Uncut elements, which have a positive constant distance value, are colored in light green. On the other hand, green and red are used to color the positive and negative distance regions of cut elements.

Moreover, it is worth mentioning the treatment of complex intersection patterns and their implications in the calculation of such discontinuous distance function. Fig. 2 qualitatively describes an example of these cases. By inspecting one of the elements intersected by two bodies at the same time, it is observable that the multiple intersection pattern is approximated as plane which is not coincident with the neighbours' intersections, generating a discontinuity in the distance field. This kind of complexities together with the discussion and implementation of the techniques to deal with them are extensively described in [35].

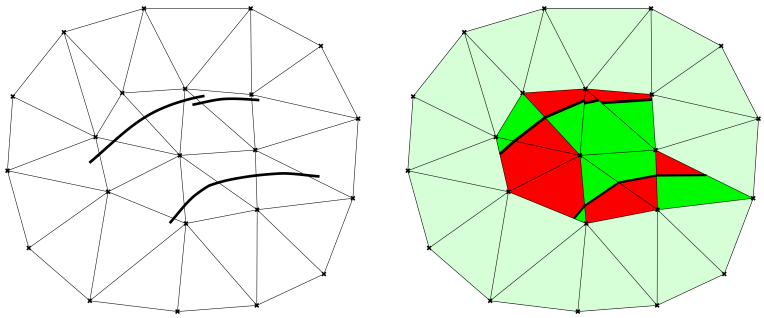

Figure 2: Discontinuous distance function. Body without internal volume (left) and discontinuous distance representation (right). Red and green portions of the cut elements indicate the positive and negative discontinuous distance regions. Light green denotes the non-intersected elements.

Finally, it is interesting to comment that all the geometries that could be represented by a continuous distance field could also be represented by a discontinuous one as well. From a mathematical point of view, this is explained by the fact that the space of continuous distance functions is contained in the discontinuous one. Indeed, any continuous distance algorithm firstly computes the elemental body-skin intersections, which altogether conform the discontinuous distance field, for then obtaining the continuous one by avoiding the jumps between neighbour elements.

2.5. Body fitted slip boundary condition

Even though this work mainly focuses on embedded fluid formulations, body fitted discretizations are used as reference solution during the implementation and validation of the presented formulation. This subsection describes the technique used for the imposition of the slip boundary condition when dealing with body fitted discretizations.

In this case, the body fitted slip condition is imposed in a "MultiFreedom Constraint" (MFC) fashion [36]. This approach is based on the rotation of the assembled stiffness matrix of the problem. This means that for each slip node, a local coordinate system is defined such that one component (two in 3D) is tangent to the slip boundary while the other one is orthogonal to it. Thus, the Cartesian velocity components u_x and u_y (as well as u_z in 3D) turn into a normal velocity component u_n together with a tangential one $u_{t,1}$ (besides another one $u_{t,2}$ in 3D).

In what follows, the methodology is described for a sample problem of the form $\mathbf{Ku} = \mathbf{f}$. Note that the same procedure holds for the N-S assembled system of equations if the rotation operations are applied to the velocity DOFs disregarding the pressure ones, which is to apply the rotation to the velocity DOFs submatrices.

Therefore, starting from the assembled system of equations $\mathbf{Ku} = \mathbf{f}$, the unknowns vector $\mathbf{u}$ can be split into two sets. As shown below, one set contains the slip boundary nodes DOFs $\mathbf{u}_\Gamma$, while the other contains the rest of the nodal

unknowns $\mathbf{u_{int}}$

$$\begin{pmatrix} \mathbf{K_{int,int}} & \mathbf{K_{int,\Gamma}} \\ \mathbf{K_{\Gamma,int}} & \mathbf{K_{\Gamma,\Gamma}} \end{pmatrix} \begin{pmatrix} \mathbf{u_{int}} \\ \mathbf{u_{\Gamma}} \end{pmatrix} = \begin{pmatrix} \mathbf{f_{int}} \\ \mathbf{f_{\Gamma}} \end{pmatrix} \tag{15}$$

Then, the rotation operator $\mathbf{P}$ is defined. Such operator keeps the orientation of the interior set of nodes $\mathbf{u_{int}}$ but reorients the slip boundary boundary ones $\mathbf{u_{\Gamma}}$. Thus, by defining the nodal rotation operation $\mathbf{u} = \mathbf{P}\hat{\mathbf{u}}$ the rotated slip DOFs set $\hat{\mathbf{u}}$ can be obtained. The rotation operator $\mathbf{P}$ as well as the rotation operation can be expressed as

$$\begin{pmatrix} \mathbf{u_{int}} \\ \mathbf{u_{\Gamma}} \end{pmatrix} = \begin{pmatrix} \mathbf{I} & \mathbf{0} \\ \mathbf{0} & \mathbf{R} \end{pmatrix} \begin{pmatrix} \hat{\mathbf{u}}_{\mathbf{int}} \\ \hat{\mathbf{u}}_{\mathbf{\Gamma}} \end{pmatrix} \tag{16}$$

being $\mathbf{R}$ the nodal rotation matrix and $\mathbf{I}$ the identity tensor.

The nodal rotation matrix $\mathbf{R}$ in the rotation operator $\mathbf{P}$ is computed node-by-node as

$$\mathbf{R}^n = \begin{pmatrix} v_{1,x} & v_{2,x} & n_x \\ v_{1,y} & v_{2,y} & n_y \\ v_{1,z} & v_{2,z} & n_z \end{pmatrix} \tag{17}$$

where $\mathbf{n}$ is the outwards unit normal vector and $\mathbf{v}_1$ and $\mathbf{v}_2$ are a pair of in-plane vectors orthogonal to $\mathbf{n}$. Note that this requires the computation of the unit normal vector not in the faces conforming to the slip boundary but on its nodes.

Then, the previous rotation operation is applied to the original system of equations as

$$\mathbf{P}^T\mathbf{K}\mathbf{P}\hat{\mathbf{u}} = \mathbf{P}^T\mathbf{f} \tag{18}$$

to solve for the rotated set of DOFs $\hat{\mathbf{u}}$.

Once the global system of equations has been rotated, the slip boundary condition is nothing but a strong imposition of a stick condition in the orthogonal direction to the slip boundary. In other words, the slip boundary normal velocity u_n is set to 0 (or to the mesh velocity if an ALE framework is used) by a direct substitution of the DOFs value in the rotated unknowns vector. In the same way, the rotated global stiffness matrix $\mathbf{P}^T\mathbf{K}\mathbf{P}$ rows corresponding to u_n

DOFs are all set to zero but the main diagonal component, which is set to 1 in order to enforce the imposed u_n value. The last step is the post-processing of the obtained solution $\hat{\mathbf{u}}$ to express it in terms of the original coordinate system. This is a node-by-node operation that can be easily done by computing the matrix vector product $\mathbf{u} = \mathbf{P}\hat{\mathbf{u}}$.

Finally, it is important to point out that it is not explicitly required, nor advisable for the sake of computational efficiency, to assemble the entire rotation operator. Hence, the proper implementation consists in looping the slip boundary nodes to locally perform the rotation operations by taking the assembled global system submatrices instead.

2.6. Embedded Nitsche slip boundary condition

The first formulation to impose the slip boundary condition in an embedded framework discussed in this work has been recently published by Winter et. al. in [17]. This technique has been selected to serve as reference embedded slip solution because of its accuracy and stability properties. It consists in a stabilized Nitsche imposition of the general Navier condition described as

$$(\mathbf{u} - \mathbf{g})\,\mathbf{P}^n = \mathbf{0} \tag{19a}$$

$$(\varepsilon\,([\mathbb{C} : (\boldsymbol{\nabla}^s \mathbf{u})] \cdot \mathbf{n} - \mathbf{h}) + \mu\,(\mathbf{u} - \mathbf{g}))\,\mathbf{P}^t = \mathbf{0} \tag{19b}$$

where $\mathbf{g}$ and $\mathbf{h}$ are the velocity and the tangential traction to be imposed over the boundary. As it is clearly seen, the general Navier condition is composed by a normal contribution (Eq. 19a) together with a tangential one (Eq. 19b). The normal and tangential projection matrices are denoted as $\mathbf{P}^n$ and $\mathbf{P}^t$ and can be computed as $\mathbf{P}^n = \mathbf{n} \otimes \mathbf{n}$ and $\mathbf{P}^t = \mathbf{I} - \mathbf{n} \otimes \mathbf{n}$, being $\mathbf{I}$ the identity tensor.

Note that this boundary condition behaves as a wall-law in accordance to the slip length parameter ε. Therefore, it becomes a no-slip boundary condition when $\varepsilon = 0$ and a full-slip boundary condition when $\varepsilon \to \infty$ and $\mathbf{h} = 0$.

As it is mentioned above, the imposition of the boundary condition in Eq. 19 is done by using a stabilized Nitsche method in both the normal and tangential

directions. The Nitsche imposition normal component reads as

$$\begin{aligned}\langle\frac{\mu}{\gamma h}\left(\mathbf{u_h}-\mathbf{g}\right)\mathbf{P}^n,\mathbf{w}\rangle_\Gamma-\langle\left(\mathbf{u_h}-\mathbf{g}\right)\mathbf{P}^n,\left(q\mathbf{I}+\zeta\mathbb{C}:\boldsymbol{\nabla}^s\mathbf{w}\right)\mathbf{n}\rangle_\Gamma+\\ \langle\frac{\phi_u}{\gamma h}\left(\mathbf{u_h}-\mathbf{g}\right)\mathbf{P}^n,\mathbf{w}\rangle_\Gamma\end{aligned} \tag{20}$$

while the tangential one is

$$\begin{aligned}&\langle\frac{1}{\varepsilon+\gamma h}\left(\varepsilon\left(\mathbb{C}:\boldsymbol{\nabla}^s\mathbf{u_h}\mathbf{n}-\mathbf{h}\right)+\mu\left(\mathbf{u_h}-\mathbf{g}\right)\right)\mathbf{P}^t,\mathbf{w}\rangle_\Gamma-\\ &\zeta\langle\frac{\gamma h}{\varepsilon+\gamma h}\left(\varepsilon\left(\left[\mathbb{C}:\left(\boldsymbol{\nabla}^s\mathbf{u_h}\right)\right]\cdot\mathbf{n}-\mathbf{h}\right)+\mu\left(\mathbf{u_h}-\mathbf{g}\right)\right)\mathbf{P}^t,\left(\boldsymbol{\nabla}^s\mathbf{w}\right)\cdot\mathbf{n}\rangle_\Gamma\end{aligned} \tag{21}$$

being γ a penalty constant and $\zeta\in\{-1,1\}$. If $\zeta=-1$ the Nitsche formulation is adjoint inconsistent. According to the original authors, the adjoint inconsistent formulation enjoys improved inf-sup stability for any value of the penalty constant γ [17]. Even though optimal convergence is not guaranteed for the velocity L^2-error in this case, the adjoint inconsistent formulation has been used in this work owing to its better stability properties. ϕ_u is a stabilization constant defined as

$$\phi_u=\mu+\rho\|\mathbf{u}\|h+\frac{\rho}{\Delta t}h^2 \tag{22}$$

More information regarding the implementation, stability analysis and validation can be found in [17].

2.7. Embedded discontinuous slip boundary condition

This subsection proposes an alternative approach to impose the slip boundary condition on embedded boundaries. The new technique is based on the use of the discontinuous Ausas FE space [37] in the intersected elements. The imposition of the slip BC is achieved by integrating the mass conservation equation by parts so that the condition is weakly applied on the embedded boundary. This is completed with the use of a penalty approach for the imposition of the same constraint in the momentum equation.

The Ausas FE space has been successfully used for representing the discontinuities arising from the resolution of two-phase flow problems in [37] and [38]. A similar idea is used in the present case, but aiming to capture the jump in

both velocity and pressure fields coming from the immersion of an object in the fluid domain.

Furthermore, it is important to remark that the capability of representing discontinuities makes it possible to consider those cases in which the embedded body has no internal volume (e.g. boat sails). This ability overcomes the limitation of the slip formulation presented in the previous subsection [17] or other no-slip formulations in the literature [13], which require at least one internal node to perform the imposition.

On the other hand, it is also worth mentioning that the Ausas shape functions are conforming with the standard FE space ones used in the neighbouring elements. This property is extremely advantageous from the implementation point of view, since no modification is required in the blending elements (the ones that are attached to any split element), allowing them to use the standard FE space with no modification.

To describe the main geometrical features of the Ausas FE space, the same sample splitting pattern used by the original authors in [37] is taken and presented again in Fig. 3. By inspecting the shape functions representation derived from the previous splitting pattern (Fig. 4) the next two main attributes can be noted:

- The shape function values along an intersected edge are constant. For instance, in the example depicted in Fig. 3, the shape function at the intersection points Q and P takes the same value than in A on the green side. On the other hand, on the red side the value at the intersection point Q takes the same value than in C. The same can be said for P and B.

- The shape function gradients are approximatively null in the intersection normal direction. This property makes them suitable for the application of the slip BC, since the absence of tangential stresses corresponds to a zero gradient in the normal direction.

Concerning the null tangential stress requirement, it is approximatively satisfied inside the elements because of the inability of the Ausas FE space to

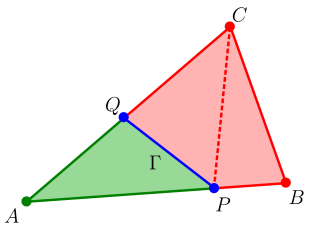

Figure 3: Partition of a triangular finite element ABC into subelements following the interface PQ (source [37]).

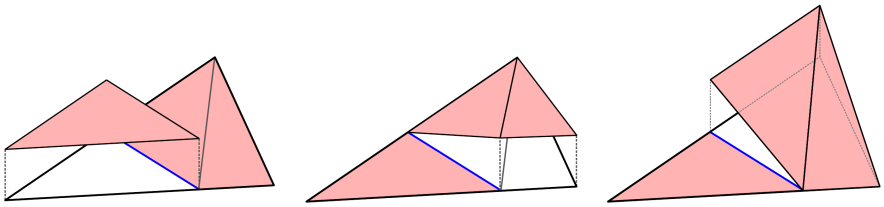

(a) N_A (b) N_B (c) N_C

Figure 4: Triangle shape functions for the Ausas finite element space and the splitting pattern in 3 (source [37]).

capture the gradient in the intersection normal direction. Moreover, the zero shear stress Neumann boundary condition is imposed over the interface cuts as

$$\langle \mathbf{w}, p_h \mathbf{n} - \mathbf{t_h} \rangle_\Gamma = \langle \mathbf{w}, 2p_h \mathbf{n} - (\mathbb{C} : \boldsymbol{\nabla}^s \mathbf{u_h}) \cdot \mathbf{n} \rangle_\Gamma = 0 \tag{23}$$

If the Neumann boundary condition in Eq. 23 is added to the original boundary term coming from the integration by parts of the momentum equation, both contributions can be condensed in a unique boundary term

$$\langle \mathbf{w}, 2p_h \mathbf{n} - \mathbb{C} : \boldsymbol{\nabla}^s \mathbf{u_h} \cdot \mathbf{n} \rangle_\Gamma + \langle (\mathbb{C} : \boldsymbol{\nabla}^s \mathbf{u_h}) \cdot \mathbf{n} - p_h \mathbf{n} \rangle_\Gamma = \langle \mathbf{w}, p_h \mathbf{n} \rangle_\Gamma \tag{24}$$

which substitutes the boundary term in the functional depicted in Eq. 12.

Two additional strategies are adopted for the imposition of the non-penetrability constraint. The first one is to integrate by parts one of the mass conservation equation terms as

$$-(q, \boldsymbol{\nabla} \cdot \mathbf{u_h})_\Omega = (\boldsymbol{\nabla} q, \mathbf{u_h})_\Omega - \langle q, \mathbf{u_h} \cdot \mathbf{n} \rangle_\Gamma \tag{25}$$

As a consequence, a boundary term which includes the normal projection of the velocity appears. Hence, a weak imposition of the non-penetrability condition can be done by dropping this term only in the embedded interface boundary integrals. It is important to recall that this new boundary term must be considered in all the other domain boundaries.

The second strategy to impose the non-penetrability requirement is to add a penalty constraint to the normal projection of the velocity in the momentum conservation equation. This new term reads as

$$\langle \kappa \mathbf{w}, \mathbf{u_h} \mathbf{n} \otimes \mathbf{n} \rangle_\Gamma = 0 \tag{26}$$

where κ stands for the consistent penalty coefficient computed as

$$\kappa = \frac{C_{Pen} \left(\frac{\rho h^d}{\Delta t} + \mu h^{d-2} + \rho \|\mathbf{u}\| h^{d-1} \right)}{A_{int}} \tag{27}$$

where C_{Pen} is a constant, which is set to 10.0 in all the cases discussed in this work, d is the working dimension (2 in 2D and 3 in 3D) and A_{int} is the intersection area.

To sum up, the proposed formulation implements the two requirements of a slip boundary condition, which are null normal projection of the velocity and null tangential stress, in a weak sense by:

- integrating the mass conservation equation by parts and dropping the boundary term on the elemental cuts.
- using a penalty constraint to the normal component of the velocity.
- using the discontinuous FE space presented in [37] in the intersected elements together with a null tangential stress Neumann boundary condition imposition in the elemental cuts.

3. Validation examples

This section is intended to describe the benchmarking task, which has been conducted to test and compare all the implemented functionalities with low and

high Re in both 2D and 3D. Hence, the geometry, boundary conditions and simulation settings that are required to reproduce the presented experimental cases are detailed together with the discussion of the obtained results. A relation of the presented benchmark cases and a brief motivation is listed below

- 2D flow inside a ring: to obtain the convergence rates of the presented formulation and assess its behaviour with faceted approximations of curved geometries.
- 2D squeezing flow: to obtain the convergence rates of the presented formulation in the high Re and inviscid scenarios.
- 2D elbow with internal wall: to test the presented formulation when modelling embedded flow discontinuities at low Re number.
- 2D flow around cylinder: to compare the three slip formulations when modelling bodies with internal volume at high Re number.
- 2D flow around vertical plate: to prove the capabilities of the presented discontinuous embedded formulation when modelling volumeless immersed bodies.
- 2D divergent channel with moving cylinder: to preliminary assess the capabilities of the discussed embedded formulations when facing moving boundaries problems.
- 3D elbow with internal wall: to test the presented discontinuous embedded formulation in a 3D case.
- 3D flow around two boat sails: to show a potential industrial application of the presented discontinuous embedded formulation.

3.1. 2D flow inside a ring

This first example has two main objectives. The first one is to obtain the velocity and pressure convergence rates of the presented formulation. The sec-

ond one is to assess the behaviour of the method when dealing with polygonal approximations of curved boundaries.

As pointed out in [16], the imposition of slip boundary conditions on curved boundaries might become an issue when such faceted approximations are used. In [16], the method of manufactured solutions is applied to check the convergence of a Stokes formulation together with a Nitsche-based slip boundary condition imposition. According to the authors, it can be observed that velocity approximations almost vanish at the boundary vertices of the curve approximation when convergence does not hold. They associate this behaviour to the fact that the slip boundary condition tends to impose the velocity field to be parallel to each face of the polygonal approximation, which is to say to vanish at the common vertex between faces.

The geometry of the problem, which is equivalent to the one discussed in [16], consists of two concentric cylinders generating an interior fluid cavity. Thus, the fluid domain Ω can be described as $(x, y) \in \mathbb{R}^2 : \ 0.25 \leq x^2 + y^2 \leq 1$ (a ring with inner radius equal to 0.5 m and outer radius equal to 1.0 m). Initially, the fluid is at rest, but a movement is induced by imposing a constant angular velocity in the outer cylinder. The analytical solution which corresponds to the application of a slip BC over the inner boundary is

$$v_r = 0 \tag{28a}$$

$$v_\Theta = r \tag{28b}$$

$$p = \frac{\rho}{2}\left(r^2 - 1\right) \tag{28c}$$

The dynamic viscosity μ and density ρ are 1.0Kg/m^3 and 1e-3Kg/ms. Regarding the boundary conditions, the velocity and pressure fields are fixed to the analytical solution along the outer contour. The BDF2 time scheme is used for the time discretization. 10 time steps of 200s (Δt) are computed, resulting in a total simulation time of 2000s, which guarantees that a steady-state solution is reached.

A centred structured mesh is used in all the cases. The domain is meshed without taking the inner cylinder into account, which is represented by a radial

discontinuous distance function. The elemental sizes for each refinement level as well as the radial and perimeter subdivisions are collected in the Table 1. Fig. 5a depicts the mesh after the first refinement (Mesh 1 in Table 1) while Fig. 5b details the intersection pattern which results from the distance function. As it can be observed, the pink region in Fig. 5b represents the fluid domain whereas the light blue one is the interior part of the inner cylinder.

Table 1: 2D flow inside a ring mesh refinement settings.

	Mesh 0	Mesh 1	Mesh 2	Mesh 3	Mesh 4	Mesh 5	Mesh 6
Element size [m]	0.1428	0.06667	0.03448	0.01754	0.00884	0.00444	0.00223
Radial divisions	7	15	29	57	113	225	449
Perimeter divisions	21	43	85	169	337	673	1345

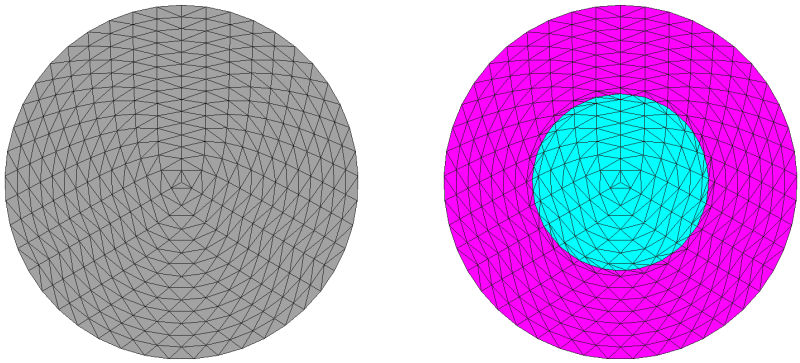

(a) Mesh 1 capture. (b) Distance intersection pattern.

Figure 5: 2D flow inside a ring.

Table 2 collects the $L^2(\Omega)$-norm of both the velocity and pressure errors. Figures 6 and 7 display a convergence rate of the order of $h^{3/2}$ for both the velocity and the pressure unknowns. These results are in line with the ones obtained by Ausas et al. in [37] and are perfectly expected due to the worse

interpolation properties of the modified discontinuous FE space used in the intersected elements.

Table 2: 2D flow inside a ring velocity and pressure error norms.

	Mesh 0	Mesh 1	Mesh 2	Mesh 3	Mesh 4	Mesh 5	Mesh 6
$\|\mathbf{u}-\mathbf{u_h}\|_{L^2(\Omega)}$	0.351411	0.245968	0.15305	0.075216	0.030324	0.011653	0.004751
$\|p-p_h\|_{L^2(\Omega)}$	0.149445	0.080384	0.050110	0.025281	0.010379	0.004016	0.001641

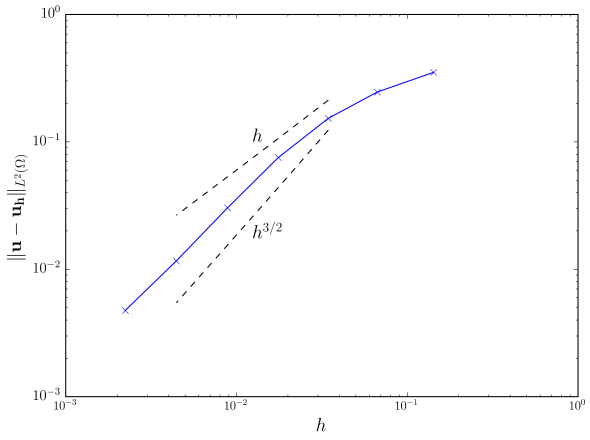

Figure 6: 2D flow inside a ring. Velocity convergence rates. Solid lines represent the obtained results. Dashed lines represent h and $h^{3/2}$ convergence rates.

Finally, the velocity and the pressure fields are shown in Fig. 8 for the coarsest, intermediate and finest meshes. The coarsest mesh solution is far from the expected one, while the intermediate and finest meshes give a good approximation. As observed by Urquiza et. al. in [16], the coarsest mesh is very inaccurate, however upon mesh refinement the method converges to the analytical solution.

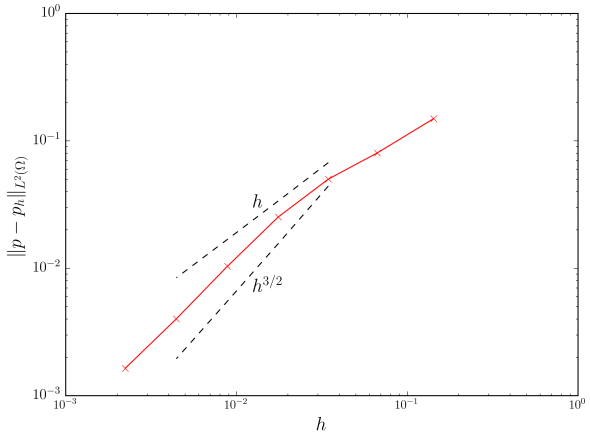

Figure 7: 2D flow inside a ring. Pressure convergence rates. Solid lines represent the obtained results. Dashed lines represent h and $h^{3/2}$ convergence rates.

3.2. 2D squeezing flow

The aim of this test is to evaluate the convergence rates of the presented formulation for the transient high Re and inviscid scenarios. To that purpose, the squeezing flow between two moving plates with time dependent velocity is solved. However, only the top half of the domain is considered. The symmetry condition is used to verify the proposed embedded slip formulation.

After such simplification, the problem geometry consists of a rectangular shaped domain of 1x0.25m (width x height). A space and time dependent velocity equal to

$$v_y = \begin{cases} -2tx & x < 0.5 \\ -2(1-x)t & x \geq 0.5 \end{cases} \tag{29}$$

is imposed to the top plate. Since a symmetric solution is expected, the horizontal velocity component v_x is also fixed to 0 on the top edge midpoint. A free outlet condition is assumed in both the left and right edges. Zero dynamic viscosity and unit density are considered in the inviscid limit case. For the high Re scenario, the dynamic viscosity is set to 5e-9Kg/ms to have a Re number equal to 10^5Re.

The reference solutions ($\bar{\mathbf{u}}$,$\bar{p}$) for the convergence study are computed using an extremely fine body-fitted mesh. On the other hand, Table 3 collects the mesh settings (horizontal and vertical edges subdivisions) for the embedded cases. Note that the embedded meshes height is 0.3 m and a distance field $d(x, y) = y$ is used to get an equivalent computational domain.

Table 3: 2D squeezing flow mesh refinement settings.

	Mesh 0	Mesh 1	Mesh 2	Mesh 3	Mesh 4
Element size [m]	0.008333	0.004166	0.002083	0.001042	0.000521
Vertical divisions	31	61	121	241	481
Horizontal divisions	120	240	480	960	1920

The BDF2 scheme is used for the time discretization. A total of 3 time steps of 1e-5s (Δt) are run in both test cases. A previous convergence study using the body fitted solution proved that the selected time step value is small enough to ensure that the error in space dominates the time dependent one for the reference mesh.

Tables 4 and 5 collect the $L^2(\Omega)$-norm of both the velocity and pressure errors for the 10^5Re and inviscid scenarios. As it can be observed from figs. 9 and 10, the velocity and pressure convergence rate is around h^2 for the 10^5Re case. On the other hand, figs. 11 and 12 show that in the inviscid limit the convergence rates for both velocity and pressure fields deteriorate to h. This behaviour might be explained by the fact that the penalty constant κ (Eq. 27) converges to a finite value in the inviscid limit. This can be seen as, in the assumption that $A_{int} \approx h^{d-1}$, $h \to 0$ and $\mu \to 0$, the penalty coefficient κ converges to $C_{Pen}\rho\|\mathbf{u}\|$. We observe however that to the best of our knowledge classical convergence estimates are not valid for the inviscid scenario.

Finally, the obtained velocity and pressure fields are shown in Figs. 13 and

Table 4: 2D squeezing flow velocity and pressure error norms (10^5Re).

	Mesh 0	Mesh 1	Mesh 2	Mesh 3
$\|\bar{\mathbf{u}} - \mathbf{u_h}\|_{L^2(\Omega)}$	8.22085e-7	5.78898-7	1.22989e-7	3.33973e-8
$\|\bar{p} - p_h\|_{L^2(\Omega)}$	3.39966e-2	2.38613e-2	4.60455e-3	8.71143e-4

Table 5: 2D squeezing flow velocity and pressure error norms (inviscid).

	Mesh 0	Mesh 1	Mesh 2	Mesh 3	Mesh 4
$\|\bar{\mathbf{u}} - \mathbf{u_h}\|_{L^2(\Omega)}$	8.83323e-7	7.52714e-7	2.6534e-7	1.41099e-7	7.18316e-8
$\|\bar{p} - p_h\|_{L^2(\Omega)}$	3.65597e-2	3.10994e-2	1.06083e-2	5.45133e-3	2.76408e-3

14 for the reference body fitted and embedded solutions. As it is clearly seen, no differences can be detected between the two solutions, showing that the formulation also works for the transient high Re and inviscid limit cases.

3.3. 2D elbow with internal wall

The purpose of this test is to assess the correctness and performance of the presented discontinuous formulation, as well as its capability of modelling embedded flow discontinuities. For that aim, the presented theoretical example, which has analytical solution, has been solved with several mesh refinement levels. The obtained solution is compared with the body fitted and literature ones.

This example was firstly proposed in [39], and consists of a 90° curved 2D pipe conforming to an elbow shape. A zero-thickness wall is placed inside the curved pipe, generating two separated fluid ducts with varying cross section area. The geometry of the problem is depicted in Fig. 15.

The fluid properties are selected such that the Re number has unit value.

Taking the radius of each one of the ducts as reference length, such unit Re number can be achieved by setting density ρ to 1Kg/m^3, dynamic viscosity μ to 1Kg/ms and a constant inlet velocity u_x of 1m/s. Furthermore, the pipe walls are assumed to be no-slip and the pressure is fixed to zero on the outlet.

Concerning the time discretization, the BDF2 time scheme is used with a time step (Δt) of 10^{-2}s. The total simulation time is 1s, which is enough to reach a stationary solution.

The meshes employed were as similar as possible to the ones used for the reference solution. Thus, four structured triangular grids were used. The number of elements employed on each grid, together with the reference ones in [39], are presented in Table 6.

Table 6: 2D elbow with internal wall number of elements for different refinement levels.

Mesh	Reference	Present work
Coarse	2400	2300
Medium	9600	8900
Fine	38400	36200
Very fine	153600	147000

In the following, the performance of the proposed discontinuous embedded formulation is assessed. First of all, the new formulation results are presented. After that, the obtained solution is compared with the expected and body-fitted ones and a different discontinuous formulation proposed in [39]. Besides that, the results of the mesh refinement study are also discussed.

Fig. 16 shows the presented discontinuous formulation velocity and pressure fields for the medium mesh. As expected, the contraction generated by the wall in the right duct induces a pressure gradient, which turns to a flow acceleration

that preserves the inlet flow rate. The opposite behaviour can be observed in the left duct, since the cross section remains constant.

The medium mesh results obtained with the presented discontinuous embedded formulation are compared with the body fitted solution and with the reference ones in Fig. 17a. Such comparison is done by means of the y-component velocity distribution at the outlet. At a first glance, an extremely good correlation can be seen. However, minor differences can be observed in the values close to the wall. Taking into account that the meshes are quite similar but not perfectly equal between the three cases, sufficiently good agreement is found to asseverate that the proposed discontinuous embedded formulation correctly solves the posed problem.

A mesh refinement study is done by using the proposed embedded formulation. The y-component of the outlet velocity is used again as the comparison magnitude. As it can be observed in Fig. 17b, the results in the region close to the internal wall improve as long as the mesh is refined.

Table 7 shows the maximum y-component velocity values in the outlet of both sides of the membrane. As it pointed out in [39], considering that the flow is parabolic in both sides of the internal wall, it can be proven that the analytical maximum velocity must be 1.5m/s and 3m/s in the left and right ducts. Taking these two values as a reference, the absolute errors are also computed and presented in Table 7. The values converge to the expected solution as the mesh is refined.

3.4. 2D flow around cylinder

The fourth benchmark is the inviscid incompressible flow around a cylinder. The purpose of this test is to compare the two described embedded slip formulations with the body fitted one. This problem has analytical solution, so the three presented solutions are also compared with the theory.

The problem geometry consists of a cylinder with radius 0.1m, which has its centre point in (0.0,0.0)m, placed inside a 10.0x4.0m channel. The bottom left corner of the channel is located in (-2.0,-2.0)m. Note that, the channel size is

Table 7: 2D elbow with internal wall. Maximum vertical velocity in the outlet using different meshes [m/s].

	$\lvert\mathbf{v_y}\rvert^{left}_{max}$	abs. err.	$\lvert\mathbf{v_y}\rvert^{right}_{max}$	abs. err.
Expected	1.5	-	3.0	-
Coarse	1.4261	0.0739	2.7301	0.2699
Medium	1.4561	0.0439	2.8874	0.1126
Fine	1.4630	0.0370	2.9413	0.0587
Very fine	1.4759	0.0241	2.9367	0.0633

set such that the blockage coefficient is equal to the 5%. This ensures that the problem boundaries do not affect the solution around the immersed cylinder. A constant inlet is imposed at the left edge, symmetry boundary conditions are used in both the top and bottom edges and the pressure is fixed to zero at the right end edge.

Owing to the inviscid assumption, the Re number is infinite. The dynamic viscosity μ is set to 0.0Kg/ms, the density ρ to 1Kg/m^3 and the inlet velocity to 1m/s. Concerning the time discretization, the BDF2 scheme is used with a time step Δt of 10^{-2}s and a total simulation time of 1s.

A distance modification criterion is used to avoid badly defined intersections that might compromise the convergence of the embedded cases. Thus, when the distance value is less than 0.01% the elemental size (i.e. the zero of the level set function is close to a node) the distance field is corrected by slightly modifying it as it is explained in the next paragraph. This makes it possible to avoid the use of small-cut stabilization techniques [14].

For the continuous distance case (Nitsche formulation), this is only needed in those elements where the fluid portion is almost null. Thus, the threshold

tolerance is set with negative sign to deactivate the almost empty elements. On the contrary, this is not a problem when using the presented discontinuous formulation, since both sides of the level set are assembled and solved. Therefore, an absolute threshold criterion is enough to ensure that the distance value is not too close to 0.

Fig. 18 describes the problem geometry as well as the auxiliary meshing subregions, which mesh sizes are collected in Table 8.

Table 8: 2D flow around cylinder mesh settings.

Region	A	B	C	D
Mesh size [m]	0.05	0.025	0.01	0.001

The pressure coefficient (C_p) is selected as reference comparison magnitude. From a known pressure in the far field p_∞, the pressure coefficient can be computed in each node as

$$C_{p,i} = \frac{p_i - p_\infty}{\frac{1}{2}\rho\|\mathbf{v}_i\|^2} \tag{30}$$

The C_p analytical solution for the presented case can be found in [40] and is computed as

$$C_p(\theta) = 1 - 4\sin^2(\theta) \tag{31}$$

Figure 19 describes the evolution of the pressure coefficient according to the angle θ, being $\theta = 0$ in the cylinder downstream point. At first glance, the evolution of the body fitted C_p has almost perfect agreement with the analytical solution. With regard to both embedded formulations, no differences can be observed in the evolution of C_p if they are compared with the body fitted solution.

However, if it is zoomed in on the downstream region ($\theta \approx 0$) minor disparities with respect to the analytical solution are observed (Fig. 20a). In this region, the C_p values are slightly below the expected ones, confirming that

both embedded formulations are a bit more diffusive than the body fitted one. Such numerical diffusivity results in an artificial flow separation located in the leeward region of the cylinder.

On the other hand, it is worth to comment something on the results obtained for either the top ($\theta \approx \pi/2$) or bottom ($\theta \approx 3\pi/2$) parts of the cylinder. By a close-up inspection, it can be noted that minor oscillations appear in both embedded solutions (Fig. 20b). Such oscillations are much less significant in the Nitsche solution and are most likely to be associated to poorly-conditioned intersection patterns. Furthermore, the the Ausas FE space solution presents a staggered pattern, reflecting the interpolation properties of the method.

The expected and obtained peak C_p values are presented in Table 9 for each one of the presented solutions. The relative errors of such values with respect to the analytical solution are collected in Table 10. As it has been pointed before, significant differences between the different formulations can only be found in $\theta = 0$ region. In his location, the C_p relative error of the Nitsche formulation is 11.3% while the discontinuous Ausas formulation one is 12.29%.

Table 9: Inviscid incompressible 2D flow around a cylinder. C_p peak values.

Formulation	C_p			
	$\theta = 0$	$\theta = \frac{\pi}{2}$	$\theta = \pi$	$\theta = \frac{3\pi}{2}$
Theory	1.0	-3.0	1.0	-3.0
Body fitted	0.9823	-3.0179	1.0017	-3.0146
Embedded (Nitsche)	0.8870	-3.0180	1.0011	-3.0191
Embedded (Ausas)	0.8771	-3.0185	1.0000	-3.0053

Finally, the velocity field contour lines surrounding the cylinder are shown in Fig. 21. If both embedded solutions are compared with the body fitted one,

Table 10: Inviscid incompressible 2D flow around a cylinder C_p. Peak values relative errors.

Formulation	C_p rel. err. [%]			
	$\theta = 0$	$\theta = \frac{\pi}{2}$	$\theta = \pi$	$\theta = \frac{3\pi}{2}$
Body fitted	1.77	0.60	0.17	0.49
Embedded (Nitsche)	11.30	0.60	0.11	0.64
Embedded (Ausas)	12.29	0.62	0.0	0.18

the previously commented small flow separation in the downstream region of the cylinder becomes evident. Such artificial flow separation is slightly more significant in the discontinuous formulation case, which is something that can be expected due to the worse interpolation properties of the Ausas FE space.

3.5. 2D flow around vertical plate

The objective of this test is to assess the capability of the proposed discontinuous formulation to model bodies without internal volume at high Re numbers. As commented before, the viscous-slip approach makes sense when the wall viscous effects are negligible. This is an assumable simplification in convection dominated flows which is to say, in high Re number flows. To this end, the flow around a vertical plate problem is solved using the presented discontinuous embedded formulation. The performance of the obtained solution is analysed by comparing with the body-fitted solution.

In this case, the channel geometry and boundary conditions are the same as in the previous example. Concerning the immersed object, a vertical plate, which has a height and center as 0.2m and (0.0,0.0)m respectively, is placed instead of the cylinder. Fig. 22a depicts the problem geometry together with the auxiliary mesh regions.

It is worth mentioning that the plate has an almost zero thickness of 10^{-4}m

in the body fitted case. If a zero-thickness plate is considered, the nodal normals in both plate tips are zero. This results in a zero-column in the rotation matrix (Eq. 17) that causes the body-fitted slip formulation to fail. Furthermore, the body fitted plate tips are modified to be sharp ended so that the effect onto the fluid flow properly represents a thin plate (Fig. 22b).

On the other hand, no special treatment for the plate tips were done in the embedded case. Even though this induces a non-physical jump, it has been proven in [23] that these discontinuities are negligible, meaning that no special procedure is required in the elements containing the plate endpoints.

Taking the plate height as reference length, the fluid properties and flow conditions are set such that the Re number is 10^6Re. Therefore, the density ρ is 1Kg/m^3, the dynamic viscosity μ is 2e-7Kg/ms and a constant inlet value u_x of 1m/s is imposed in the left edge of the domain. Concerning the time discretization, the BDF2 scheme is used again with a time step Δt equal to 10^{-2}s and a total simulation time of 20s. The bad intersections correction that has been explained in the previous subsection is applied as well.

With regard to the space discretization, Table 11 shows the mesh size in each one of the meshing subdivisions depicted in fig 22a.

Table 11: 2D flow around vertical plate mesh settings.

Region	A	B	C	D
Mesh size (m)	0.05	0.025	0.01	0.0025

The pressure coefficient (Eq. 30) is the main comparison magnitude. However, since this problem has a periodic solution, a time averaged C_p is used instead. Thus, the time averaged C_p values considering the results from simulation time 10s to 20s are used for the results assessment.

Fig. 23 presents the evolution of the time averaged C_p values along the plate. First of all, it has to be said that the disparity of the results in both plate

ends is associated to the plate thickness discrepancies. Note that the plate has the ideal zero thickness in the embedded case but it is modelled considering an infinitesimal thickness in the body fitted one. Preliminary tests showed that such disparities are even larger if a rectangular body-fitted plate (without the modified sharp tips) is analysed.

Disregarding the plate edges disparities, the embedded formulation results have quite good agreement with the reference body fitted ones in the upstream side of the plate. The C_p value in the stagnation point ($y = 0$ m) is 0.996 for the body fitted case and 0.978 for the discontinuous embedded formulation. Considering that the pressure coefficient in the stagnation point is expected to be equal to 1.0, a relative error of 0.4% and 2.2% is obtained.

Concerning the results in the downstream side, a similar trend but with differences in the obtained values is observed. Having a look onto the downstream C_p peak values, the body fitted one is -4.201 meanwhile the discontinuous embedded one is -4.060, representing a relative difference of 3.36%.

Besides that, it is interesting to comment on the staggered distribution of the discontinuous embedded solution. Once again, this behaviour is explained by the worse interpolation properties of the Ausas FE space, which always yields a continuous interpolation in one of the element subdivisions.

As in the previous example, Fig. 24 shows the body fitted and embedded velocity contour lines for a period of oscillation. Comparing both velocity distributions, it can be said that both solutions are in good agreement in the plate surroundings. However, the aforementioned poorer interpolation properties of the Ausas FE space are noted in the downstream side of the plate, where a sharp staggered velocity distribution is observed. These results are in accordance with the results that have been discussed in the C_p distribution.

3.6. 2D divergent channel with moving cylinder

This example is intentionally set to show two of the main potential applications of the presented formulations. On one hand, it is intended to prove the capabilities of embedded formulations in dealing with large moving boundaries

without remeshing. On the other hand, it is also good to assess how the pseudo-compressibility term, added to the mass conservation equation, can alleviate the convergence problems in those cases where the pressure tends to blow up.

Thus, the problem geometry (Fig. 25) consists of a 2D divergent channel together with a moving cylinder of radius 0.1m immersed in the divergent region. This problem tries to reproduce, in an extremely simplified manner, a valve which regulates the flow by opening according to the pressure value.

Complementary, Eq. 32 describes the horizontal displacement of the cylinder centre point for a given period of oscillation T. In this case, the period is set to 5s. Assuming that the cylinder origin is placed in (x_{cyl},0)m coordinates, the x-component of the cylinder centre point can be computed as

$$x_{cyl} = 0.15 + 0.5(1 - abs(sin(\frac{2.0\pi t}{T}))) \tag{32}$$

yielding a maximum displacement of 0.5m.

For the sake of simplicity, the cylinder movement is considered to be quasi-static. This means that the cylinder skin velocity is assumed to be null and is not included in the fluid problem.

The fluid density ρ is unitary and the dynamic viscosity μ is 10^{-3}kg/ms. Besides, the pseudo-compressibility constant c (speed of sound velocity) is reduced to 10^{6}m/s. Such choice is enough to guarantee that the problem remains well defined even though isolated fluid cavities appear. A constant unit inlet is imposed at the left edge, slip boundary conditions are set at the the channel top and bottom walls and the pressure is fixed to zero at the right edge.

The BDF2 time scheme is used again with a time step of 0.1s. The mesh employs approximately 60k elements featuring an average size of 5e-3m.

Finally, the same correction to bad intersections explained in the previous examples is used. However the distance threshold is increased to 1% the element size due to the larger possibility of having poor intersections owing to the large boundary movement.

In the next lines, the solutions obtained with both embedded formulations discussed in this work are compared.

First of all, it is important to mention that both embedded slip formulations discussed in this paper are capable of solving the posed problem. Taking into account the fact that solving this test case using a body fitted formulation might require remeshing due to the extremely large displacement, the utility of embedded techniques in the resolution of this kind of problems is proven.

If the solution between the proposed discontinuous embedded formulation is compared to the Nitshche one, no differences can be observed. Fig. 26 and Fig. 27 collect such comparison for the velocity and pressure fields for a quarter of a period of oscillation. As it can be observed in these sequence of snapshots, the pressure in the inlet channel becomes larger as long as the cylinder approximates to it. Similar behaviour can be noted in the velocity field, which peak values appear in the cylinder surroundings in order to keep the flow rate.

3.7. 3D elbow with internal wall

This example is a 3D extension to the previously presented one and is aimed to prove that the presented formulation also works in 3D. For that purpose, the problem is solved using the presented discontinuous formulation as well as the Nitsche one. Note that the Nitsche formulation is not capable of handling immersed objects without internal volume such as the membrane separating the two ducts. As a consequence, two different Nitsche cases are solved: one for each one of the ducts. This can be easily done by switching the distance function sign. As reference solution for the comparison, the same case is solved using the body fitted formulation.

With regard to the geometry, the one described in Fig. 15 is extruded to have a unit thickness value. To preserve the 2D flow pattern, a symmetry boundary condition is imposed at both sides of the 3D domain. Moreover, the other boundary conditions remain as in the original 2D case. Concerning the rest of the problem settings, the original 2D ones are used again.

For the sake of computational effort, the 3D equivalent mesh to the medium refinement level described in Table 6 is used. Thus, all meshes are conformed by equal order pressure-velocity linear tetrahedra.

The main comparison magnitude is the outlet velocity (z-component in the 3D case). Even though there are no 3D reference results, the analytical values in [39] have been taken as reference solution since the flow is expected to behave as in the 2D case because of the symmetry conditions.

Table 12 shows the midplane vertical velocity component values for the three described formulations. The results show good agreement with the expected results for all the studied cases. Similar relative errors can be observed, independently of the formulation used, indicating that the new formulation is performing on par with well established approaches.

Table 12: 3D elbow with internal wall. Midplane maximum vertical velocity in the outlet [m/s] formulations comparison.

	$\lvert\mathbf{v_y}\rvert^{left}_{max}$	rel. err.	$\lvert\mathbf{v_y}\rvert^{right}_{max}$	rel. err.
Expected	1.5	-	3.0	-
Body fitted	1.446	3.60	2.9081	3.06
Embedded (Nitsche - left)	1.4368	4.21	-	-
Embedded (Nitsche - right)	-	-	2.8936	3.55
Embedded (Ausas)	1.4851	0.99	2.9007	3.31

The obtained velocity and pressure fields are compared in Fig. 28 and Fig. 29. Recall that in the Nitsche formulation case, each one of the ducts needs to be computed separately. As it can be observed, the obtained flow distribution is in good agreement with the 2D one (Fig. 16a) and no differences can be observed between the different solutions. Regarding the pressure field, the body fitted (Fig. 29a) and Nitsche (Fig. 29c and 29d) formulations have a remarkable similarity. In general terms, this affirmation can be extended to the discontinuous embedded formulation (Fig. 29b) since only minor perturbations, which

are associated to the intersected elements modified FE space, can be observed in the elbow curvature region.

3.8. 3D flow around two boat sails

The last example shows the application of the new method to a complex double sided geometry. The model chosen here describes a two boat sails setting (Fig. 30). No reference solution of any type is available for the problem at hand so that the example simply represents a proof-of-concept application of the proposed technique in a volumeless scenario. Here the sail geometry is imported directly from a .stl file, and the solution is performed without any preprocessing step thus proving our point on the robustness of the proposed approach.

The two sails, which height is approximately 4m, are placed inside a 7x9x16m channel. A constant inlet velocity u_x of 3.6m/s (7 knots) is set. The pressure is fixed at the outlet and a slip boundary condition is set in the other channel boundaries. The BDF2 time discretization scheme is used with a time step Δt of 0.1s and a total simulation time of 20s. Concerning the space discretization, a mesh conformed by approximately 4.8M linear tetrahedral elements is used.

Unlike in the previous examples, where the distance could be computed analytically, a robust distance calculation algorithm is required [35]. Fig. 31 depicts the reconstructed geometry, which matches the input shape quite well except at the sails boundary, where a saw-toothed shape is obtained as a consequence of the employed distance algorithm, which cannot represent "partial" intersections, in other words, the elements that are not completely intersected by the sails skin.

Despite the lack of reference results makes a comparison of the obtained solution with alternative formulations impossible, the results appear to be convincing. The formulation is capable of representing the discontinuities between the windward and leeward sides within one element. A positive overpressure appears in the windward region of the sails (Fig. 32b) while suction appears in the leeward one (Fig. 32a) without any sign of numerical overshoots or under-

shoots. As it is expected, the obtained velocity field (Fig. 33) is tangent to the sails surface as corresponds to the imposition of the slip BC (Fig. 34).

4. Conclusion

The aim of this work is to study the imposition of the slip boundary condition in the viscous incompressible Navier-Stokes equations in combination with boundary non-conforming mesh discretizations. This objective is achieved on the one hand, by discussing the imposition of the slip boundary condition in body fitted formulations by means of an MPC fashion technique. On the other hand, two different formulations for the embedded boundary case were studied, one based on a Nitsche imposition and another one based on the use of the modified Ausas FE space.

The former one, which relies on the imposition of a Navier-Slip boundary condition using a stabilized Nitsche method, is intended to be used in those cases in which the immersed object has a well defined internal volume, meaning that its skin can be described with a continuous distance function. The latter, which is proposed by the authors, modifies the FE space in the intersected elements to use the aforementioned Ausas discontinuous shape functions set. The convergence of the presented method is confirmed as well as its capability of representing bodies without internal volume. This interesting feature, which makes possible to solve CFD analyses of slender structures, is successfully proved in the simulation of the 2D/3D elbow with internal wall, the 2D flow around a vertical plate and the flow around two boat sails cases.

Apart from that, it is also important to stress the fact that cases with high Re number have been solved (Re=∞ and Re=10^6), obtaining a good agreement with the expected results. These results are crucial for the extension of the proposed technique to real application cases, where the viscous-slip approach can be used instead of the boundary layer mesh plus no-slip condition combination.

Regarding the accuracy of the obtained results, the body fitted solution is in general terms always better than the embedded ones. If the two studied embed-

ded approaches are compared, both methods have a similar level of accuracy, being the Nitsche method slightly more precise in some particular cases. This is perfectly expectable according to the worse interpolation properties of the modified Ausas FE space.

Besides that, the capability of the discussed embedded formulations of solving large boundary movements problems is proven with the resolution of the 2D divergent channel with moving cylinder example. Furthermore, it has to be stressed that the addition of the pseudo-compressibility term in the mass conservation equation prevents the pressure to blow up in those cases where the pressure is only defined up to a constant. This feature is exploited here to solve a problem where the flow is close to be interrupted. In addition, this capability would make possible to solve isolated fluid cavities, likely associated to to bad intersections coming from complex distance fields.

To sum up, it can be said that the correctness of all the implementations is proven. Regarding the discussed embedded slip formulations, for those bodies with well-defined internal volume, the optimal choice is concluded to be the stabilized Nitsche formulation, already published in [17], due to its slightly better accuracy and performance. However, the discontinuous embedded formulation presented by the authors arises as a feasible alternative for the analysis of bodies without internal volume, which could not be represented otherwise.

Finally, it is interesting to pinpoint the further capabilities that are still pending to be explored, such as the extension to more complex large moving boundary problems, which would require a robust initialization algorithm to be applied when topology changes occur, or the Fluid-Structure Interaction analysis of membrane and shell structures. Furthermore, it could also be interesting to investigate alternatives (e.g. Nitsche) to enhance the interface boundary condition imposition in the presented discontinuous embedded formulation.

Acknowledgements

The research was partly supported by the International Graduate School of Science and Engineering (IGSSE) through the project ATMOPACE and the European Comission (EC) through the project ExaQUte (H2020-FETHPC-2016-2017-800898). The Spanish Ministry of Economy and Competitiveness (Ministerio de Economia y Competitividad, MINECO) through the projects HIRMA (RTC-2016-4967-5) and PRECISE (BIA2017-83805-R) is also greatly acknowledged. Rubén Zorrilla and Dr. Larese gratefully acknowledge the support of the Spanish and Italian ministries respectively for their FPU grant (FPU15/03796) and Rita Levi Montalcini fellowship (Programma per Giovani Ricercatori "Rita Levi Montalcini" - bando 2016).

References

[1] C. Peskin, Numerical analysis of blood flow in the heart, Journal of Computational Physics 25 (3) (1977) 220 – 252. doi:10.1016/0021-9991(77)90100-0.

[2] C. Peskin, The immersed boundary method, Acta Numerica 112 (2002) 479 – 517. doi:10.1017/S0962492902000077.

[3] S.Osher, R. Fedkiw, Level Set Methods and Dynamic Implicit Surfaces, 1st Edition, Vol. 153 of Applied Mathematical Siences, Springer-Verlag New York, 2003.

[4] C. Hirt, A. Amsden, J. Cook, An arbitrary lagrangian-eulerian computing method for all flow speeds, Journal of Computational Physics 14 (3) (1974) 227–253. doi:10.1016/0021-9991(74)90051-5.

[5] J. Donea, A. Huerta, J.-P. Ponthot, A. Rodríguez-Ferran, Arbitrary Lagrangian–Eulerian Methods, American Cancer Society, 2004, Ch. 14. arXiv:https://onlinelibrary.wiley.com/doi/pdf/10.1002/0470091355.ecm009, doi:10.1002/0470091355.ecm009.

URL https://onlinelibrary.wiley.com/doi/abs/10.1002/0470091355.ecm009

[6] J. Cottrell, T. Hughes, Y. Bazilevs, Isogeometric analysis: toward integration of CAD and FEA, John Wiley & Sons, 2009.

[7] A. Coll, Robust volume mesh generation for non-watertigh geometries, Ph.D. thesis, Universitat Politècnica de Catalunya (7 2014).

[8] P. Frey, F. Alauzet, Anisotropic mesh adaptation for cfd computations, Computer Methods in Applied Mechanics and Engineering 194 (48) (2005) 5068 – 5082. doi:10.1016/j.cma.2004.11.025.

[9] P. Benard, G. Balarac, V. Moureau, C. Dobrzynski, G. Lartigue, Y. D'Angelo, Mesh adaptation for large-eddy simulations in complex geometries, International Journal for Numerical Methods in Fluids 81 (12) (2015) 719–740. doi:10.1002/fld.4204.

[10] F. Bertrand, P. Tanguy, F. Thibault, A three-dimensional fictitious domain method for incompressible fluid flow problems, Int. J. Num. Meth. Fluids 25 (6) (1997) 719–736. doi:10.1002/(SICI)1097-0363(19970930)25:6<719::AID-FLD585>3.0.CO;2-K.

[11] R. Löhner, J. Cebral, F. Camelli, S. Appanaboyina, J. Baum, E. Mestreau, O. Soto, Adaptive embedded and immersed unstructured grid techniques, Comput. Methods Appl. Mech. Engrg. 197 (25) (2008) 2173–2197. doi:10.1016/j.cma.2007.09.010.

[12] J. Nitsche, Über ein variationsprinzip zur lösung von dirichlet-problemen bei verwendung von teilräumen, die keinen randbedingungen unterworfen sind, Abhandlungen aus dem Mathematischen Seminar der Universität Hamburg 36 (1) (1971) 9–15. doi:10.1007/BF02995904.

[13] R. Codina, J. Baiges, Approximate imposition of boundary conditions in immersed boundary methods, Int. J. Numer. Meth. Engng. 80 (2009) 1379–1405. doi:10.1002/nme.2662.

[14] A. Massing, M. Larson, A. Logg, M. Rognes, A stabilized nitsche fictitious domain method for the stokes problem, Journal of Scientific Computing 61 (3) (2014) 604–628. doi:10.1007/s10915-014-9838-9.

[15] A. Massing, B. Schott, W. Wall, A stabilized nitsche cut finite element method for the oseen problem, Comput. Methods Appl. Mech. Engrg. 328 (2018) 262–300. doi:10.1016/j.cma.2017.09.003.

[16] J. Urquiza, A. Garon, M.-I. Farinas, Weak imposition of the slip boundary condition on curved boundaries for stokes flow, Journal of Computational Physics 256 (2014) 748–767. doi:10.1016/j.jcp.2013.08.045.

[17] M. Winter, B. Schott, A. Massing, W. Wall, A nitsche cut finite element method for the oseen problem with general navier boundary conditions, Computer Methods in Applied Mechanics and Engineering 330 (2018) 220–252. doi:10.1016/j.cma.2017.10.023.

[18] D. Kamensky, M.-C. Hsu, D. Schillinger, J. Evans, A. Aggarwal, Y. Bazilevs, M. Sacks, T. Hughes, An immersogeometric variational framework for fluid–structure interaction: Application to bioprosthetic heart valves, Computer Methods in Applied Mechanics and Engineering 284 (2015) 1005 – 1053. doi:10.1016/j.cma.2014.10.040.

[19] C. Peskin, Flow patterns around heart valves: A numerical method, Journal of Computational Physics 10 (2) (1972) 252 – 271. doi:10.1016/0021-9991(72)90065-4.

[20] C. Peskin, D. McQueen, A three-dimensional computational method for blood flow in the heart i. immersed elastic fibers in a viscous incompressible fluid, Journal of Computational Physics 81 (2) (1989) 372 – 405. doi:10.1016/0021-9991(89)90213-1.

[21] L. Zhu, C. Peskin, Interaction of two flapping filaments in a flowing soap film, Physics of Fluids 15 (7) (2003) 1954–1960. doi:10.1063/1.1582476.

[22] R. Mittal, H. Dong, M. Bozkurttas, F. Najjar, A. Vargas, A. von Loebbecke, A versatile sharp interface immersed boundary method for incompressible flows with complex boundaries, Journal of Computational Physics 227 (10) (2008) 4825 – 4852. doi:10.1016/j.jcp.2008.01.028.

[23] M. Davari, R. Rossi, P. Dadvand, Three embedded techniques for finite element heat flow problem with embedded discontinuities, Comput. Mech. 59 (2017) 1003–1030. doi:10.1007/s00466-017-1382-7.

[24] J. Hoffman, J. Jansson, C. Johnson, New theory of flight, Journal of Mathematical Fluid Mechanics 18. doi:10.1007/s00021-015-0220-y.

[25] P. Dadvand, R. Rossi, E. Oñate, An object-oriented environment for developing finite element codes for multi-disciplinary applications, Archives of Computational Methods in Engineering 17 (3) (2010) 253–297. doi:10.1007/s11831-010-9045-2.

[26] P. Dadvand, R. Rossi, M. Gil, X. Martorell, J. Cotela, E. Juanpere, S. Idelsohn, E. Oñate, Migration of a generic multi-physics framework to HPC environments, Computers & Fluids 80 (2013) 301 – 309. doi:10.1016/j.compfluid.2012.02.004.

[27] J. Cotela, R. Rossi, E. O. nate, A fic-based stabilized finite element formulation for turbulent flows, Comput. Methods Appl. Mech. Engrg. 315 (2017) 607 – 631. doi:10.1016/j.cma.2016.11.020.

[28] A. Brooks, T. Hughes, Streamline upwind/petrov-galerkin formulations for convection dominated flows with particular emphasis on the incompressible navier-stokes equations, Comput. Methods Appl. Mech. Engrg. 32 (1) (1982) 199 – 259. doi:10.1016/0045-7825(82)90071-8.

[29] T. Hughes, Multiscale phenomena: Green's function, the dirichlet to neumann formulation, subgrid scale models, bubbles and the origins of stabilized formulations, Comput. Methods Appl. Mech. Engrg. 127 (1) (1995) 387–401. doi:10.1016/0045-7825(95)00844-9.

[30] T. Hughes, G. Feijóo, L. Mazzei, J. Quincy, The variational multiscale method—a paradigm for computational mechanics, Comput. Methods Appl. Mech. Engrg. 166 (1) (1998) 3–24, advances in Stabilized Methods in Computational Mechanics. doi:10.1016/S0045-7825(98)00079-6.

[31] R. Codina, A stabilized finite element method for generalized stationary incompressible flows, Comput. Methods Appl. Mech. Engrg. 190 (20) (2001) 2681–2706. doi:10.1016/S0045-7825(00)00260-7.

[32] R. Codina, Stabilized finite element approximation of transient incompressible flows using orthogonal subscales, Computer Methods in Applied Mechanics and Engineering 191 (39) (2002) 4295 – 4321. doi:10.1016/S0045-7825(02)00337-7.

[33] R. Codina, J. Principe, O. Guasch, S. Badia, Time dependent subscales in the stabilized finite element approximation of incompressible flow problems, Computer Methods in Applied Mechanics and Engineering 196 (21) (2007) 2413 – 2430. doi:10.1016/j.cma.2007.01.002.

[34] A. Meurer, C. Smith, M. Paprocki, O. Čertík, S. Kirpichev, M. Rocklin, A. Kumar, S. Ivanov, J. Moore, S. Singh, T. Rathnayake, S. Vig, B. Granger, R. Muller, F. Bonazzi, H. Gupta, S. Vats, F. Johansson, F. Pedregosa, M. Curry, A. Terrel, Š. Roučka, A. Saboo, I. Fernando, S. Kulal, R. Cimrman, A. Scopatz, Sympy: symbolic computing in python, PeerJ Computer Science 3 (2017) e103. doi:10.7717/peerj-cs.103.

[35] D. Baumgärtner, J. Wolf, R. Rossi, P. Dadvand, R. Wüchner, A robust algorithm for implicit description of immersed geometries within a background mesh, Advanced Modeling and Simulation in Engineering Sciences 5 (1) (2018) 21. doi:10.1186/s40323-018-0113-8.

[36] C. Felippa, Introduction to finite element methods, University of Colorado, USA.

[37] R. Ausas, F. Sousa, G. Buscaglia, An improved finite element space for discontinuous pressures, Comput. Methods Appl. Mech. Engrg. 199 (2010) 1019–1031. doi:10.1016/j.cma.2009.11.011.

[38] R. Ausas, F. Sousa, S. Idelsohn, A statically condensable enrichment for pressure discontinuities in two-phase flows, Mecánica Computacional 30 (4) (2011) 175–191.

[39] S. Idelsohn, J. Gimenez, N. Nigro, Multifluid flows with weak and strong discontinuous interfaces using an elemental enriched space, International Journal for Numerical Methods in Fluids 86 (12) (2018) 750–769. doi:10.1002/fld.4477.

[40] J. Anderson, Fundamentals of Aerodynamics, 6th Edition, McGraw-Hill, 2017.

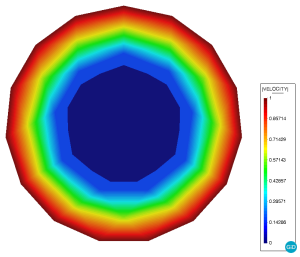

(a) Mesh 0 velocity.

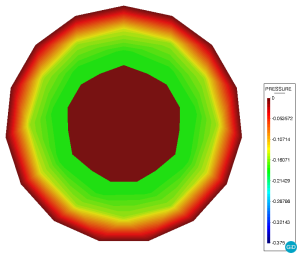

(b) Mesh 0 pressure.

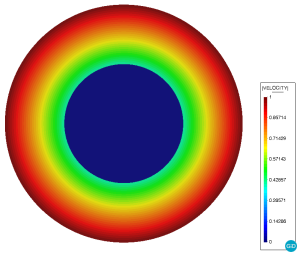

(c) Mesh 3 velocity.

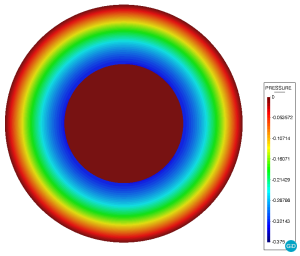

(d) Mesh 3 pressure.

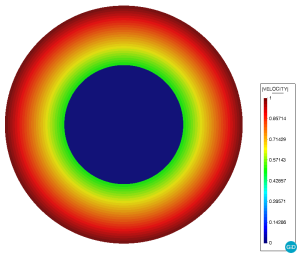

(e) Mesh 6 velocity.

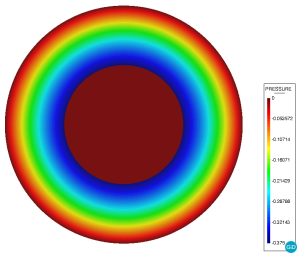

(f) Mesh 6 pressure.

Figure 8: 2D flow inside a ring. Coarsest, intermediate and finest meshes solutions.

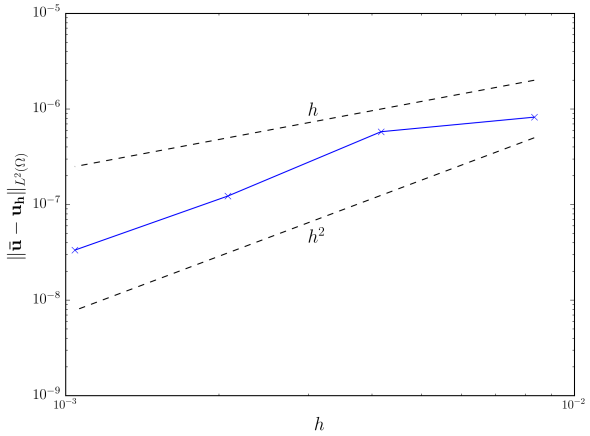

Figure 9: 2D squeezing flow. Velocity convergence rates (10^5Re). Solid lines represent the obtained results. Dashed lines represent h and h^2 convergence rates.

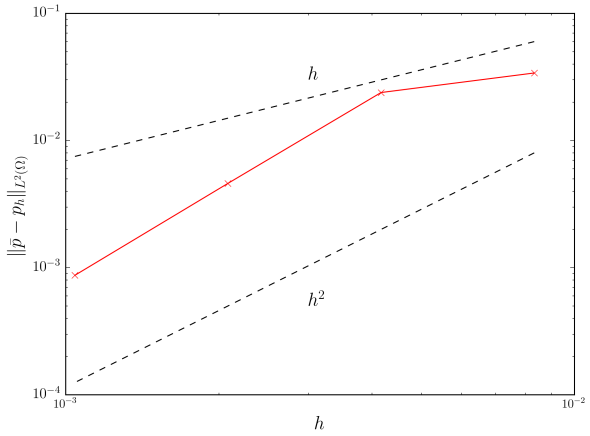

Figure 10: 2D squeezing flow. Pressure convergence rates (10^5Re). Solid lines represent the obtained results. Dashed lines represent h and h^2 convergence rates.

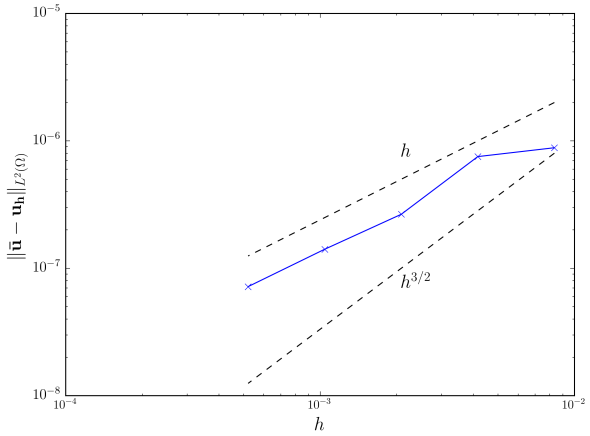

Figure 11: 2D squeezing flow. Velocity convergence rates (inviscid). Solid lines represent the obtained results. Dashed lines represent h and $h^{3/2}$ convergence rates.

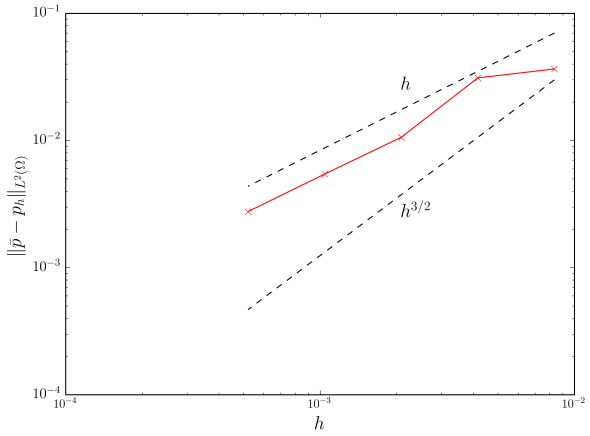

Figure 12: 2D squeezing flow. Pressure convergence rates (inviscid). Solid lines represent the obtained results. Dashed lines represent h and $h^{3/2}$ convergence rates.

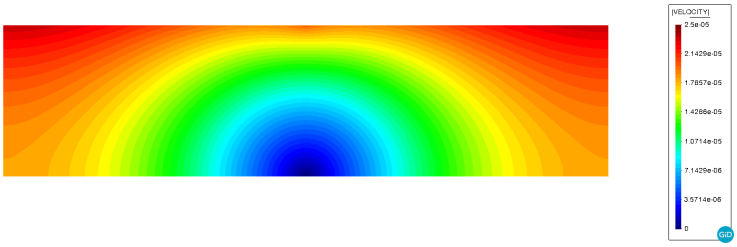

(a) Body fitted velocity.

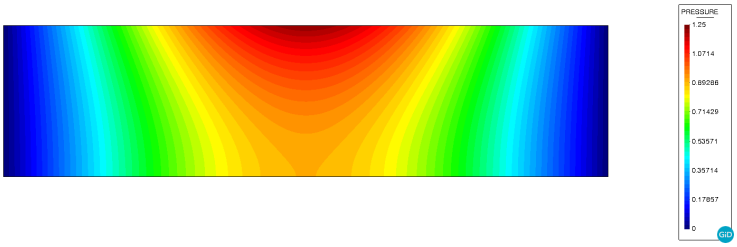

(b) Body fitted pressure.

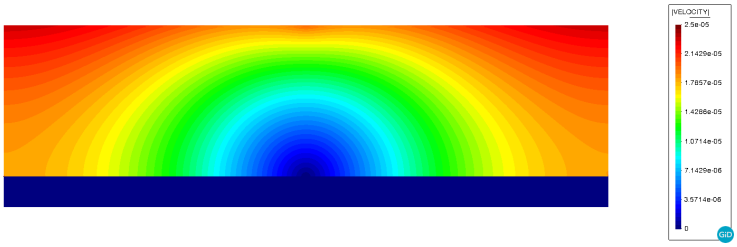

(c) Embedded mesh 3 velocity.

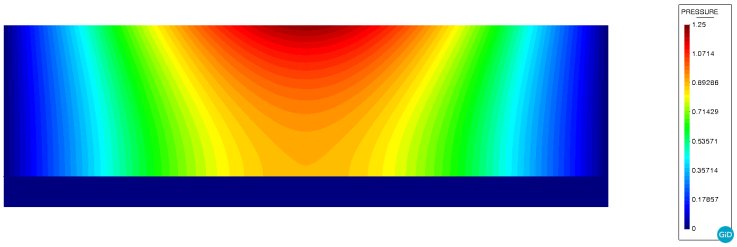

(d) Embedded mesh 3 pressure.

Figure 13: 2D squeezing flow. Reference body fitted and embedded solutions (10^5Re).

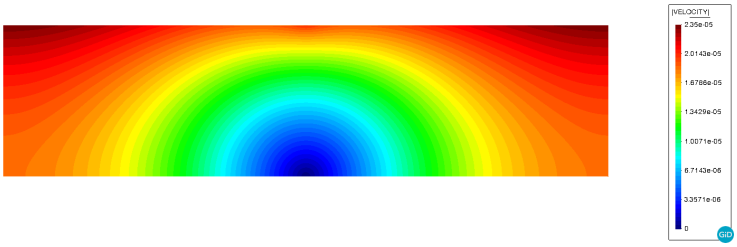

(a) Body fitted velocity.

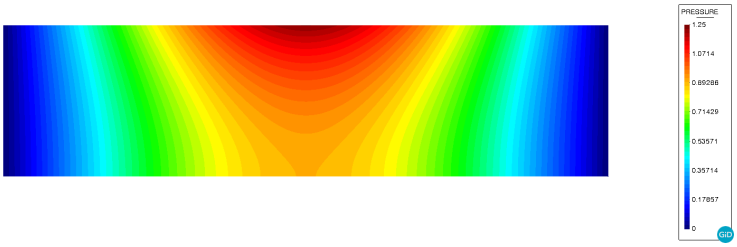

(b) Body fitted pressure.

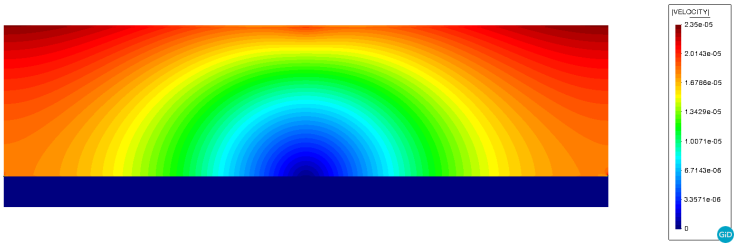

(c) Embedded mesh 4 velocity.

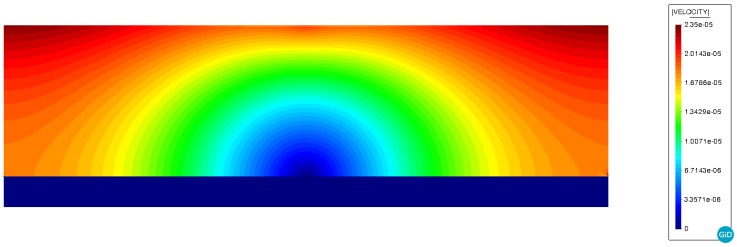

(d) Embedded mesh 4 pressure.

Figure 14: 2D squeezing flow. Reference body fitted and embedded solutions (inviscid).

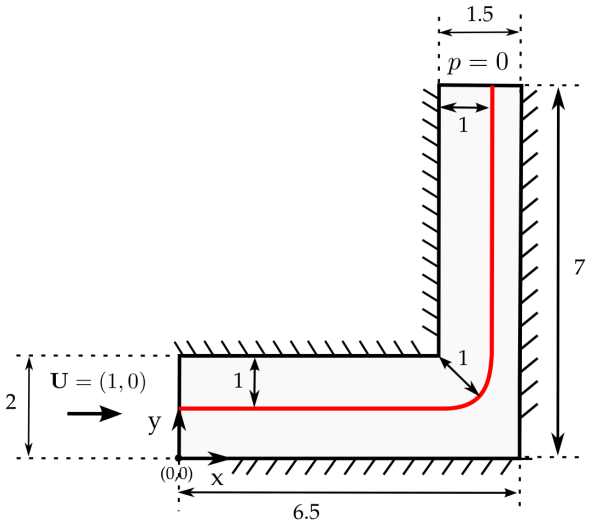

Figure 15: 2D elbow with internal wall (source [39]).

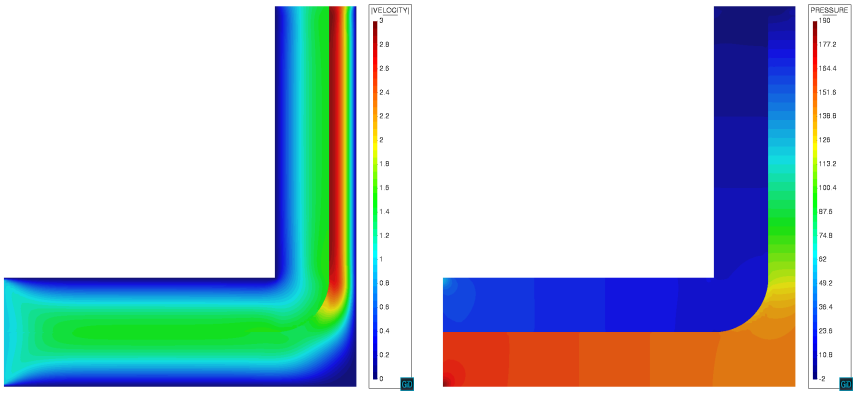

(a) Velocity modulus (m/s). (b) Pressure (Pa).

Figure 16: 2D elbow with internal wall. Discontinuous embedded solution (medium mesh).

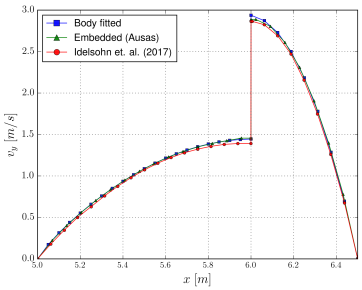

(a) Medium mesh comparison.

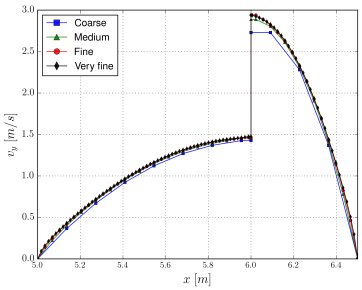

(b) Ausas solutions comparison.

Figure 17: 2D elbow with internal wall. Outlet v_y.

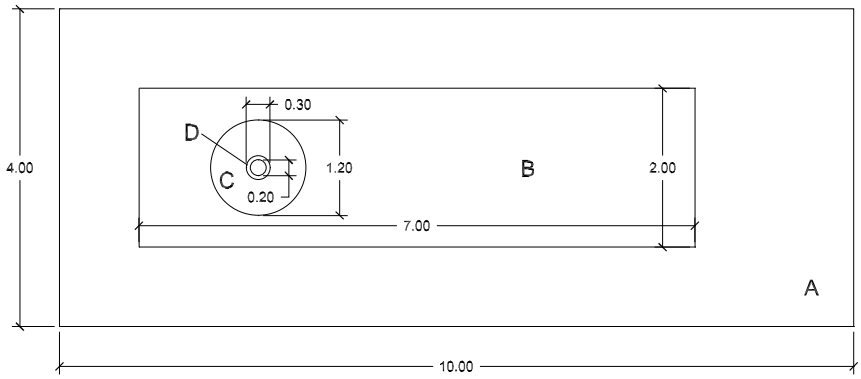

Figure 18: 2D flow around cylinder problem geometry and mesh regions.

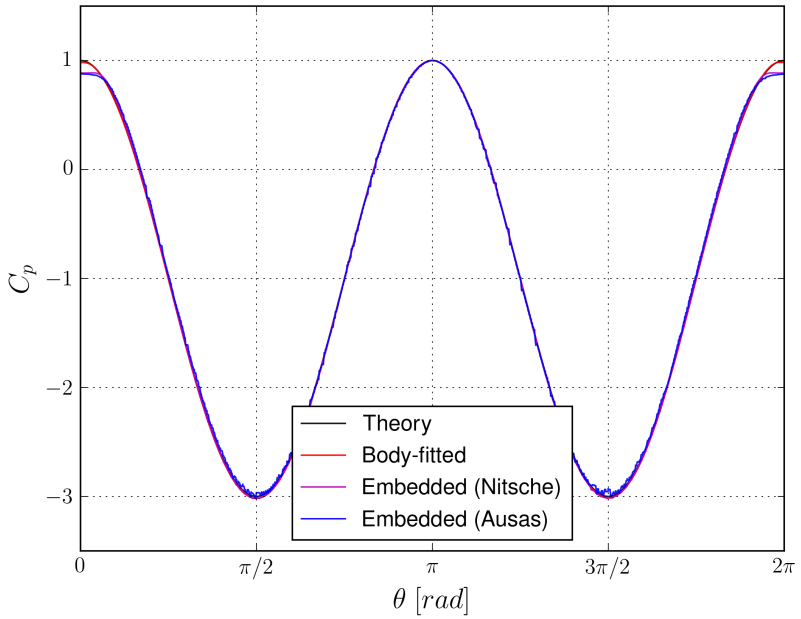

Figure 19: Inviscid incompressible 2D flow around a cylinder. $C_p(\theta)$ complete evolution.

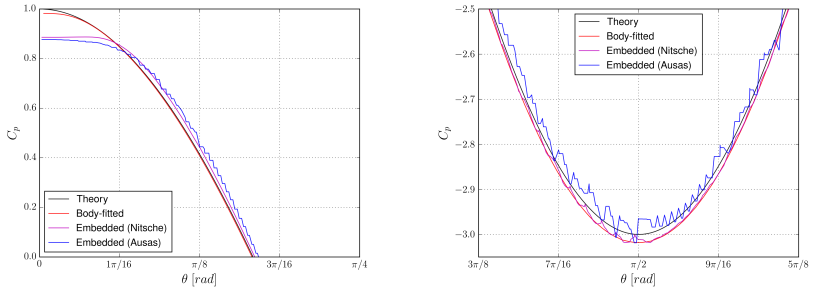

(a) $\theta \in [0, \pi/4]$ detail.

(b) $\theta \in [3\pi/8, 5\pi/8]$ detail.

Figure 20: Inviscid incompressible 2D flow around a cylinder. $C_p(\theta)$ evolution details.

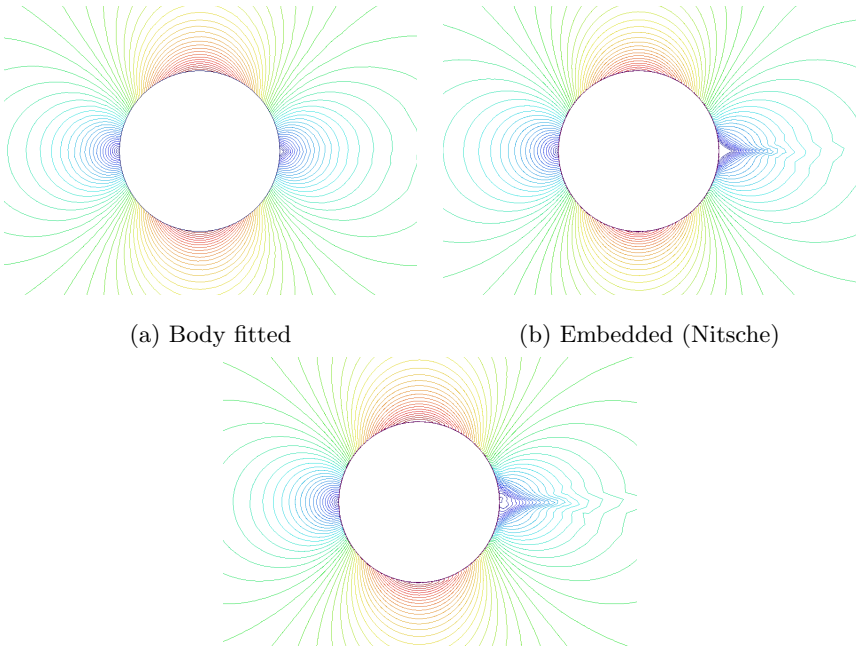

(a) Body fitted (b) Embedded (Nitsche)

(c) Embedded (Ausas)

Figure 21: Inviscid incompressible 2D flow around a cylinder. Velocity field contour lines.

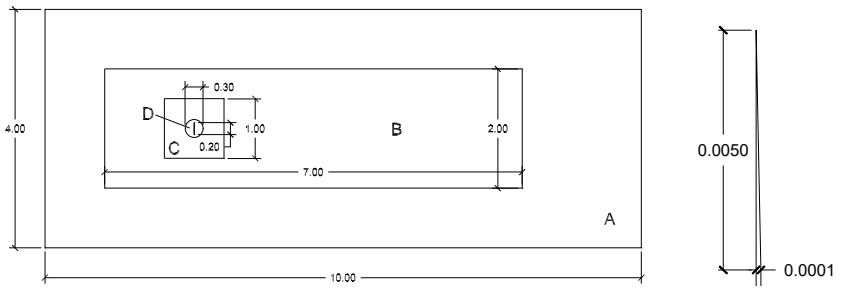

(a) Geometry and mesh regions. (b) Sharp end.

Figure 22: 2D flow around a vertical plate. Problem set-up.

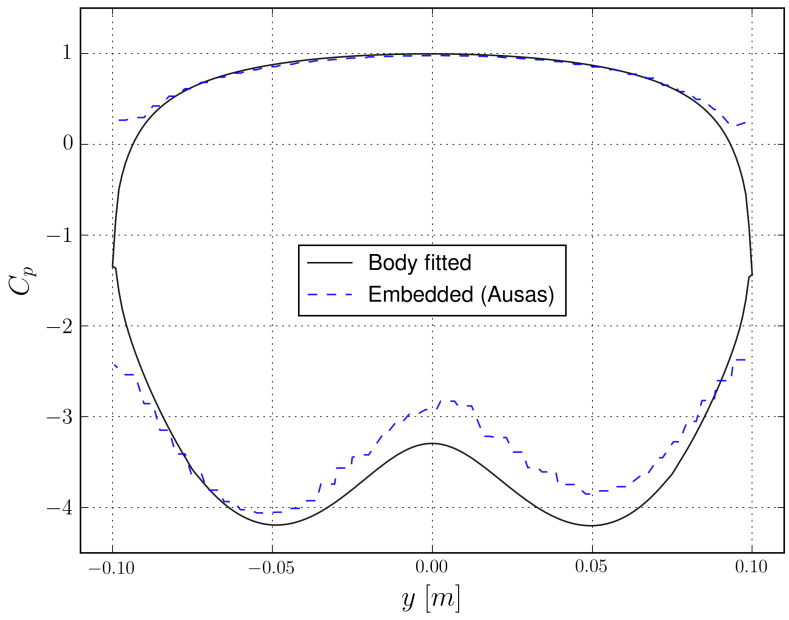

Figure 23: 2D flow around a vertical plate. C_p time averaged values.

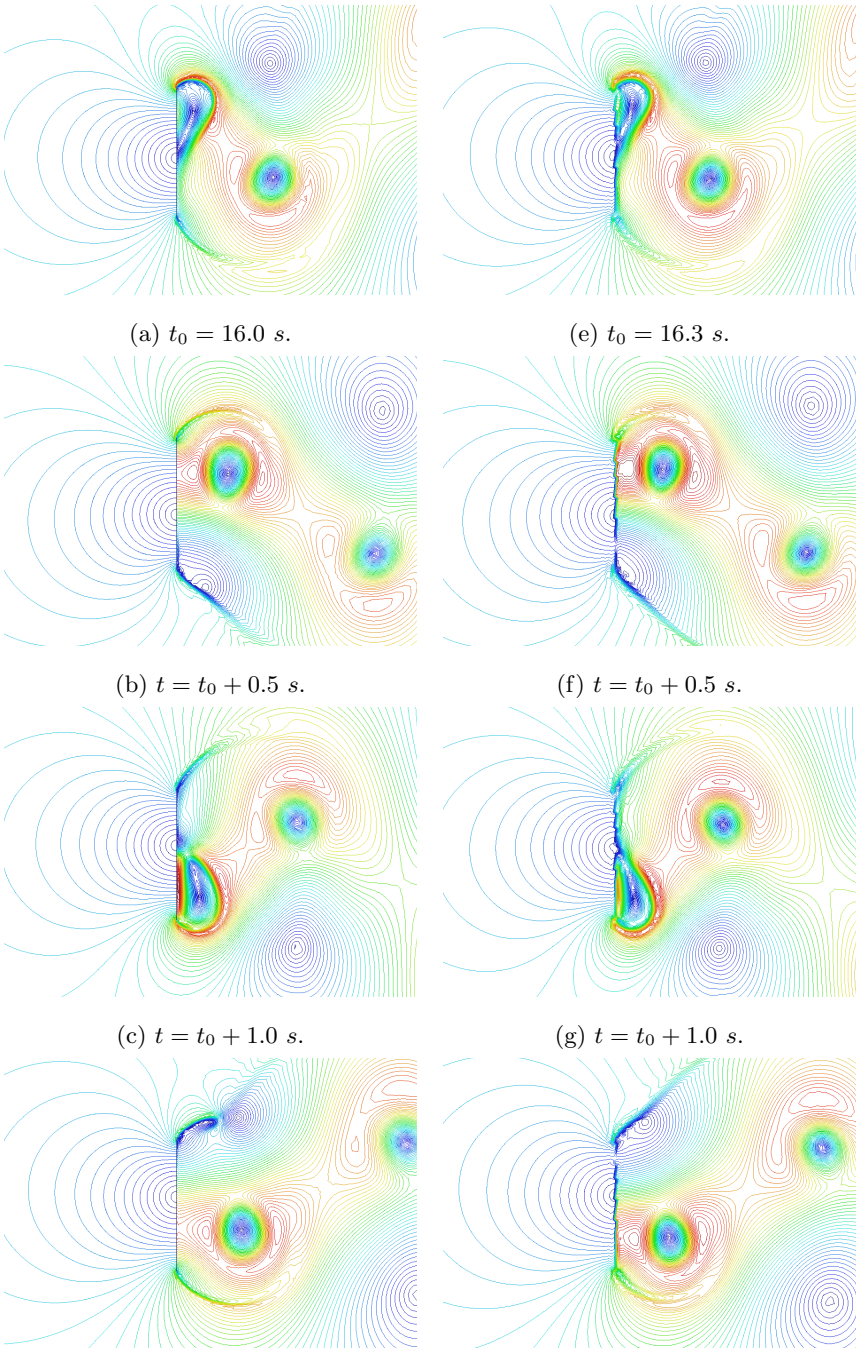

(a) $t_0 = 16.0\ s.$ (e) $t_0 = 16.3\ s.$

(b) $t = t_0 + 0.5\ s.$ (f) $t = t_0 + 0.5\ s.$

(c) $t = t_0 + 1.0\ s.$ (g) $t = t_0 + 1.0\ s.$

(d) $t = t_0 + 1.5\ s.$ (h) $t = t_0 + 1.5\ s.$

Figure 24: 2D flow around a vertical plate. Body fitted (left) and discontinuous embedded (right) formulations velocity field contour lines (results are shown for a period of oscillation in each case).

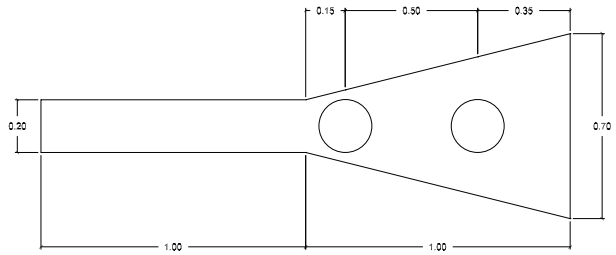

Figure 25: 2D divergent channel with moving cylinder problem geometry. The maximum and minimum displacement positions of the embedded cylinder are shown as well.

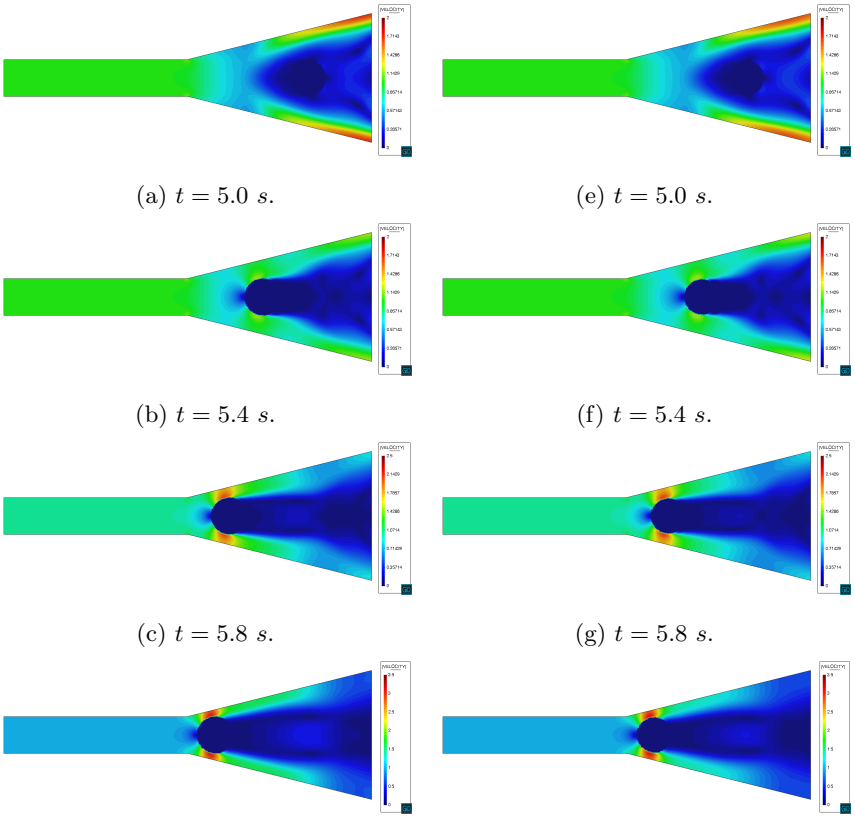

(a) $t = 5.0\ s.$ (e) $t = 5.0\ s.$

(b) $t = 5.4\ s.$ (f) $t = 5.4\ s.$

(c) $t = 5.8\ s.$ (g) $t = 5.8\ s.$

(d) $t = 6.2\ s.$ (h) $t = 6.2\ s.$

Figure 26: 2D divergent channel with moving cylinder. Embedded discontinuous (left) and continuous (right) formulations velocity field (m/s) for a quarter of a period of oscillation. Note that the contour legends are scaled between plots for a better visualization.

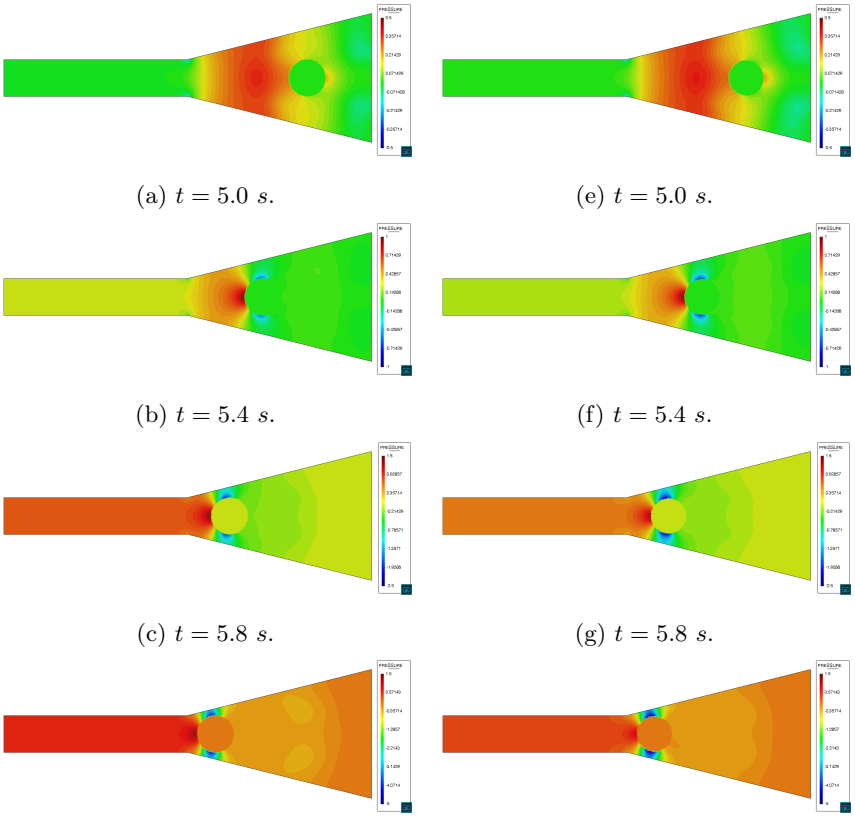

(a) $t = 5.0\ s.$ (e) $t = 5.0\ s.$

(b) $t = 5.4\ s.$ (f) $t = 5.4\ s.$

(c) $t = 5.8\ s.$ (g) $t = 5.8\ s.$

(d) $t = 6.2\ s.$ (h) $t = 6.2\ s.$

Figure 27: 2D divergent channel with moving cylinder. Embedded discontinuous (left) and continuous (right) formulations pressure field (Pa) for a quarter of a period of oscillation. Note that the contour legends are scaled between plots for a better visualization.

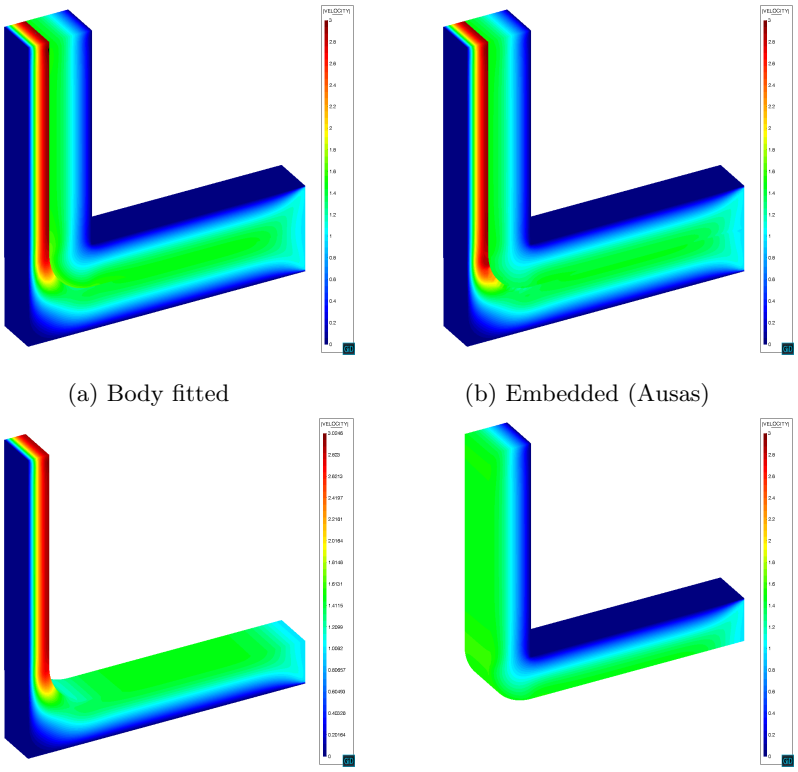

(a) Body fitted

(b) Embedded (Ausas)

(c) Embedded (Nitsche - left)

(d) Embedded (Nitsche - right)

Figure 28: 3D elbow with internal wall. Velocity modulus (m/s) comparison.

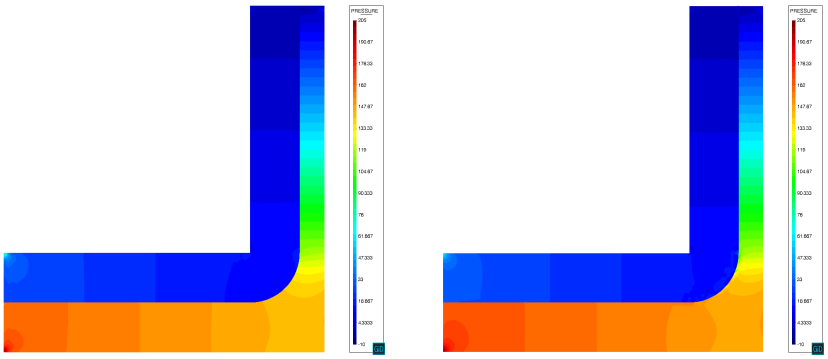

(a) Body fitted

(b) Embedded (Ausas)

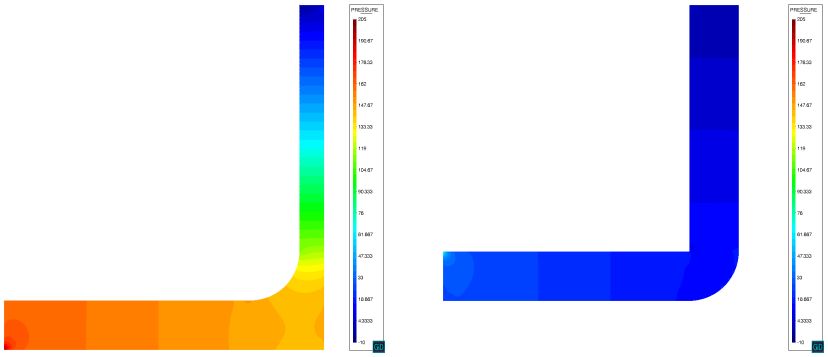

(c) Embedded (Nitsche - left)

(d) Embedded (Nitsche - right)

Figure 29: 3D elbow with internal wall. Midplane pressure (Pa) comparison.

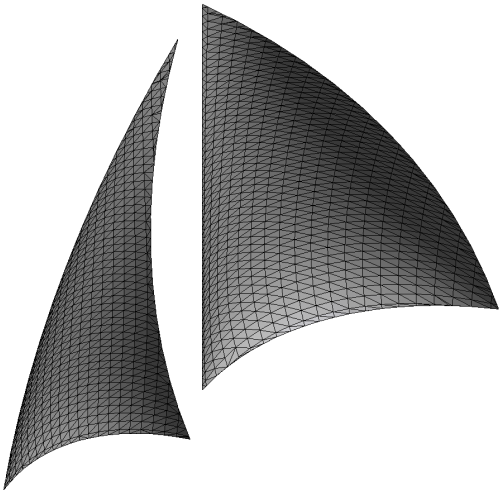

Figure 30: 3D flow around two boat sails. .stl input geometry.

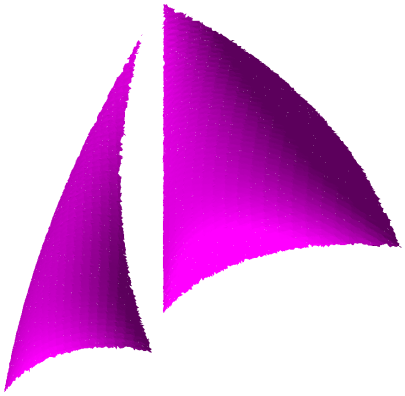

Figure 31: 3D flow around two boat sails. Element intersections from discontinuous distance field.

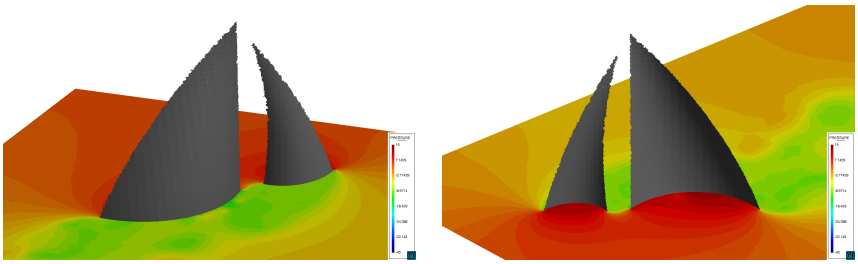

(a) Leeward view (b) Windward view

Figure 32: 3D flow around two sails. Pressure field (Pa).

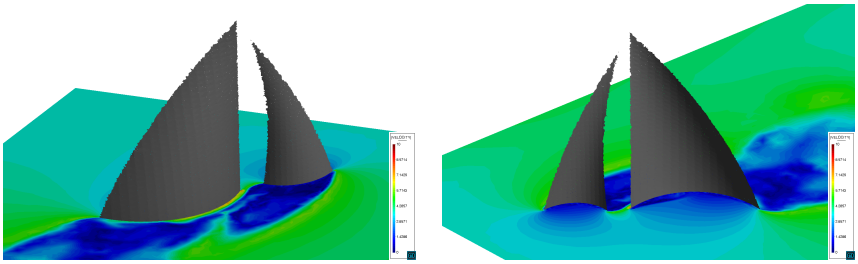

(a) Leeward view (b) Windward view

Figure 33: 3D flow around two sails. Velocity field (m/s).

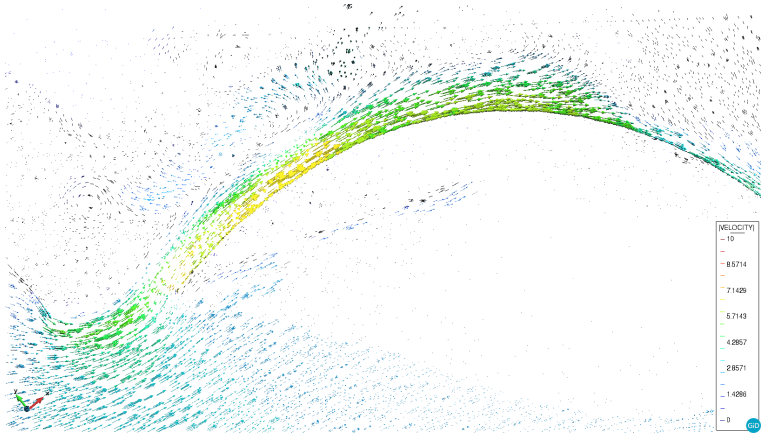

Figure 34: 3D flow around two boat sails. Velocity vector field on horizontal cut.